# Mylonite, cataclasite, and gouge: Reconstruction of mechanical heterogeneity along a low-angle normal fault: Death valley, USA

B.M. Lutz [a,b,*], G.J. Axen [b]

[a] *U.S. Geological Survey, Geosciences and Environmental Change Science Center, Denver, CO, 80225, USA*
[b] *Earth and Environmental Sciences Department, New Mexico Institute of Mining and Technology, Socorro, NM, 80501, USA*

ARTICLE INFO

ABSTRACT

The spectrum of slip behavior in crustal faults generates various rock types that can inform the mechanics of earthquake genesis. However, a single fault exposure may contain evidence of slip at various depths and temperatures due to progressive fault rock formation and overprinting during exhumation. Here, we unravel the spatiotemporal evolution of mechanical transitions along the Boundary Canyon detachment, a low-angle normal fault northeast of Death Valley, USA. Field, microstructural, and geochemical characterizations of fault rocks are compared to existing laboratory experiments and combined with a thermo-kinematic model of fault evolution. Together, these constrain the depths of mechanical transitions along the fault and reveal the evolution of earthquake nucleation zone thickness. Fault exposures from different initial paleodepths passed through the mechanical transitions during footwall exhumation, resulting in overprinting of mylonite by cataclasite and ubiquitous late formation of foliated, illite-rich gouge within the uppermost crust. We present evidence of coseismic low-angle normal fault slip (e.g., injection veins of cataclasite, laminar and grain-inertial fluidization). Coseismic slip likely nucleated at strength contrasts within the fault zone (i.e., contacts between quartzite breccia and calc-mylonite; quartz ribbons and mylonite matrix; breccia and clay gouge) at ≈ 5–9.5 km depth. Observations including mutually overprinting cataclasite/ultramylonite and exposures of pulverized gouge support that dynamic rupture propagated down-dip through the brittle-ductile transition zone (≈10–11 km depth) and up-dip through velocity-strengthening fault patches (≈0–5 km depth). Rapid fault exhumation increased the geotherm, leading to upward advection of the brittle-ductile transition and shallowing/thinning of the earthquake nucleation zone. This process may explain the rarity of large magnitude earthquakes on low-angle normal faults.

## 1. Introduction

Most crustal faults are mechanically heterogeneous due to variations in geometry, rock types, friction, fluid pressure, and temperature. Mechanical heterogeneity promotes complex slip behaviors such as dynamic rupture propagation, creep, plastic flow, and seismic tremor (Wang and Bilek, 2014; Rowe and Griffith, 2015; Collettini et al., 2019; Barnes et al., 2020). While the geometry, stress, friction, and protoliths along actual faults are required to understand seismic cycling, dynamic rupture and earthquake hazards (Steacy et al., 2005; Jia et al., 2023), only some all of these parameters are typically constrained for a given fault (Axen, 1992, 2020; Selverstone et al., 1995, 2012; Caine and Forster, 1999; Caine and Minor, 2009; Caine et al., 2010, 2017; Tesei et al., 2014; Melosh et al., 2018; Singleton et al., 2018).

Exhumed faults provide an opportunity to understand the heterogeneity and complex mechanics of faulting. Observations of naturally deformed rocks can constrain fault geometry, frictional properties, thickness, thermo-mechanical conditions of fault rock formation, slip magnitude, and slip rate. In particular, exhumed low-angle normal faults and their metamorphic footwalls can inform fault processes spanning the entire middle to upper parts of the crust (Wernicke, 1981; Davis et al., 1986, 2004, 2023; Davis, 1987; Lister and Davis, 1989; Hacker et al., 1990; Axen, 2004; Collettini and Holdsworth, 2004; Haines and van der Pluijm, 2010; Collettini, 2011; Whitney et al., 2013; Platt et al., 2015a; Spencer et al., 2016; Yin et al., 2017; Axen et al., 2018; Little et al., 2019).

However, a single fault exposure may contain evidence of slip at various depths and temperatures due to progressive fault rock formation

---

and overprinting during exhumation. The record of high temperature plastic flow in mylonite is often overprinted by brittle cataclasis, leading to formation of cataclasite, breccia, and gouge. Progressive overprinting of fault rocks renders it difficult if not impossible to constrain the nature of fault heterogeneity with depth. The geometric, thermal, and temporal evolution of a given fault is required if the heterogeneous fault rocks are to be placed into paleo-mechanical context.

Here, we integrate fault rock structure and geochemistry with the thermal and geometric evolution of the Boundary Canyon detachment (BCD), a low-angle normal fault northeast of Death Valley, USA (Fig. 1). Quartz- and calc-mylonite, various types of cataclasite, breccia, and gouge zones formed along the BCD (Fig. 1D). These fault rocks are placed into paleo-mechanical context by palinspastically reconstructing exposures of the exhumed fault in combination with existing thermal models of the fault's evolution (Lutz et al., 2021). Fault rock textures and compositions are compared with laboratory experiments to assign depth-dependent friction (static and rate-state) and map out fault mechanical transitions through time.

The multidisciplinary approach applied in this study elucidates fault mechanical heterogeneity spanning the mid-to upper-crustal column. We suggest a mechanism for initiation of coseismic, low-angle normal slip near the brittle-ductile transition zone, leading to dynamic rupture propagation through interconnected faults and ductile shear zones. We show also that upward advection of heat with footwall exhumation shallowed the brittle-ductile transition and thinned the earthquake nucleation zone. This may explain the rarity of large magnitude earthquakes on low-angle normal faults and help understand hazards of seismically active analogues (Wernicke, 1995; Rietbrock et al., 1996; Axen, 1999, 2007; Boncio et al., 2000; Abers, 2001; Floyd et al., 2001; Chiaraluce et al., 2007; Brozzetti et al., 2009; Searle, 2010; Monigle et al., 2012; Rana et al., 2013; Niemeijer and Collettini, 2014; Styron and Hetland, 2014; Anderlini et al., 2016; Vadacca et al., 2016; Little et al., 2019; Cummins et al., 2020; Pang et al., 2020; Biemiller et al., 2022).

## 2. Background: the Boundary Canyon detachment

The BCD is a low-angle normal fault located in the northern Funeral Mountains northeast of Death Valley, USA (Fig. 1). The fault accommodated top-NW directed shear and overall NW-SE directed extension in the late Miocene (Hamilton, 1988; Holm and Dokka, 1991; Hoisch and Simpson, 1993; Wright and Troxel, 1993; Applegate and Hodges, 1995; Snow and Wernicke, 2000; Lutz et al., 2021). Most of the fault exposures lie along the northern flank of the NW-SE trending footwall corrugation. Based on similar kinematics, the BCD has been correlated to the Keane Wonder fault (Hamilton, 1988; Hoisch and Simpson, 1993), which occupies the southern flank of the footwall corrugation (Fig. 1A).

The composite BCD and Keane Wonder fault surface traces separate the northern Funeral Mountains (footwall) from the Grapevine Mountains, Amargosa Valley, and Death Valley (hanging wall) (Wright and Troxel, 1993). The Funeral Mountains preserve a prograde Barrovian metamorphic field gradient (Labotka, 1980), which formed during Permian-Jurassic thrusting and burial (Snow, 1992; Stevens and Stone, 2005; Niemi, 2012; Hoisch et al., 2014; Affinati et al., 2020, 2022; Levy et al., 2021). The deep footwall in the NW contains amphibolite facies metapelite, quartzite, marble, and mylonite, whereas the shallow footwall in the SE contains greenschist to unmetamorphosed sedimentary rocks (Fig. 1A). The hanging wall is composed of relatively unmetamorphosed Neoproterozoic-Mississippian marine rocks and Miocene fanglomerate and breccia (Wright and Troxel, 1993).

Several phases of exhumation proceeded from Late Jurassic through Miocene. This paper focuses on rapid late Miocene (ca. 12-7 Ma) exhumation coincident with the main phase of slip on the BCD (Holm and Dokka, 1991; Hoisch and Simpson, 1993; Fridrich and Thompson, 2011; Fridrich et al., 2012; Lutz et al., 2021). During this time, the hanging wall was translated 35–40 km NW while the footwall was tilted
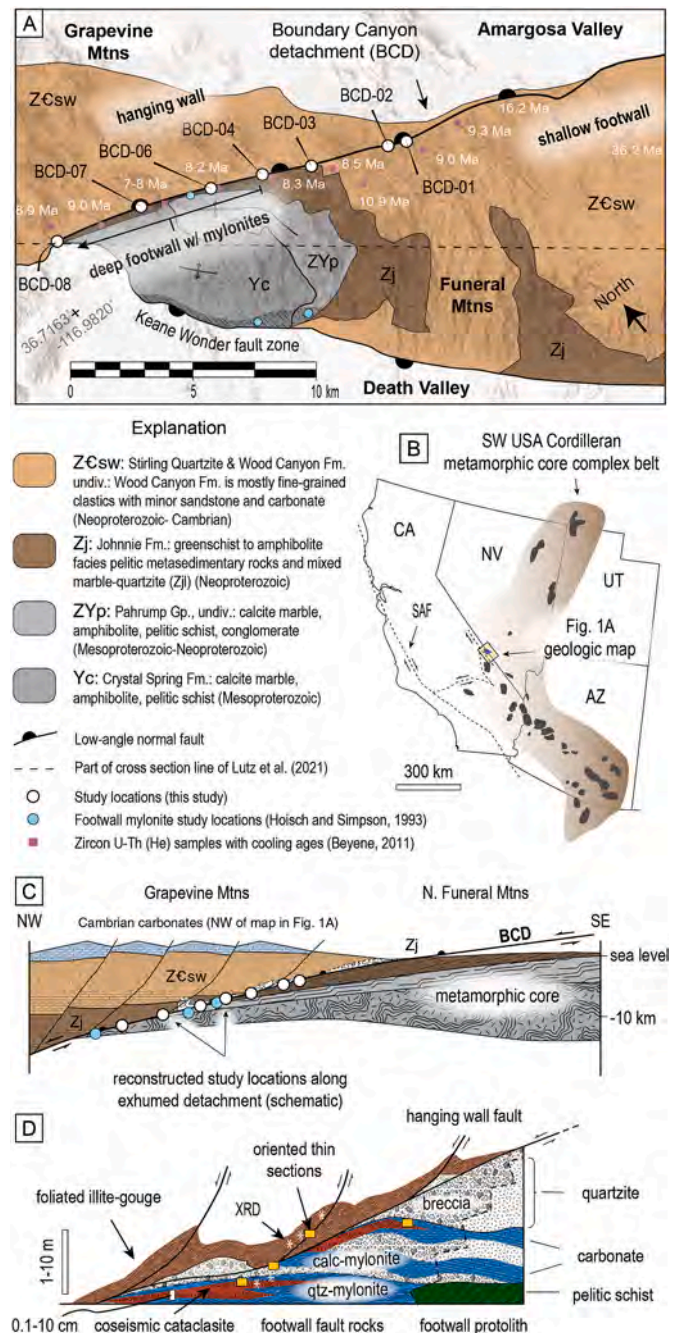


Fig. 1. Overview of study area and concepts. A) Simplified geologic map of the study area showing key outcrop locations along the Boundary Canyon detachment (BCD). Map and unit explanations are adapted from Wright and Troxel (1993) and Workman et al. (2016). B) Map of SW USA showing the location of the study area relative to the Cordilleran metamorphic core complex belt. Adapted from Wust (1986). C) Idealized structural cross section of the BCD showing hanging wall normal faults, footwall metamorphic core, and study locations along the modern BCD reconstructed to paleodepths. D) Topological section showing characteristic BCD fault rocks, their spatial scales, and their relation to hanging wall vs. footwall protoliths. qtz: quartz. Fm.: Formation. Gp.: Group. Mtns: Mountains SAF: San Andreas fault zone. Undiv.: undivided.

25–30° SE and exhumed to shallow (0–3 km) depths (Hoisch and Simpson, 1993; Lutz et al., 2021). Post-7 Ma exhumation related to transtensional faulting, E tilting, and erosion finally exposed the modern Funeral and Grapevine mountains.

Late Miocene slip along the BCD generated a heterogeneous suite of fault rocks. These are exposed discontinuously along the fault surface

trace and are the focus of this study. Due to the SE tilting of the footwall, initially deeper portions (~10–13 km depth) of the BCD containing mylonite are exposed to the NW. Initially shallower parts (~8–9.5 km depth), generally devoid of mylonite, are exposed in the SE (Fig. 1A and Table 1). The mylonite layers have been studied previously (Hoisch and Simpson, 1993; Beyene, 2011; Lima et al., 2019), but the brittle fault rocks which overprint the mylonite have received little attention.

### 2.1. Footwall mylonite

Previous work on field relations and quartz- and calc-mylonite in the Funeral Mountains laid the groundwork for this study. Wright and Troxel (1993) mapped the northern Funeral Mountains and interpreted the kilometer-scale structural relations. Hamilton (1988) initially recognized the presence of kinematically compatible mylonitic fronts in the footwalls of the Keane Wonder fault and BCD, leading him to correlate the two faults (Fig. 1A). Hoisch and Simpson (1993) later studied the mylonitic rocks from both footwalls and found consistent top-NW shear sense (hanging wall transport of 299° ± 12° azimuth).

Quartz grains within footwall quartz mylonite of the Keane Wonder fault exhibit textures consistent with bulging (BLG) and subgrain rotation (SGR) dynamic recrystallization (Hoisch and Simpson, 1993). Quartz grains formed by SGR recrystallization are ~50 μm in diameter on average. Hoisch and Simpson (1993) suggested from mineral growth modeling that initial grain size prior to annealing was <10 μm. These observations support plastic deformation at temperatures of 325–400 °C and stresses ranging from 25 to 40 MPa for the coarse grains and up to 105–125 MPa for the finer, pre-annealed grains, depending on the grain size piezometer used (Hirth and Tullis, 1992; Stipp and Tullis, 2003; Cross et al., 2017; Heilbronner and Kilian, 2017; Platt, 2023).

Calc-mylonite is present in the footwalls of the Keane Wonder fault and BCD. The calc-mylonitic front lies within the Crystal Spring Formation (unit Yc) in the Keane Wonder fault footwall and within the lower Johnnie Formation (unit Zjl) in the BCD footwall (Fig. 1A). Hoisch and Simpson (1993) reported >90% calcite grains with recrystallized grain size of 20–50 μm, abundant twinned grains, and C-axis orientations consistent with predominately pure shear (~80%). They interpreted crystal-plastic deformation between 325 and 480 °C. However, Beyene (2011) measured much smaller dynamically recrystallized calcite grains (3–9 μm). He used these observations to suggest that crystal-plastic deformation within the calc-mylonite occurred at very low temperatures (≤220 °C), based on the calibration of Ebert et al. (2008). The range of dynamically recrystallized grains suggests crystal-plastic deformation at stresses of 95–200 MPa using recent grain size piezometers (Platt and De Bresser, 2017; Platt, 2023).

Thermo-kinematic modeling indicates that modern BCD footwall exposures with mylonite experienced temperatures of 350–425 °C in the late Miocene (Lutz et al., 2021) This, in combination with the overwhelmingly top-NW shear sense indicators (Hamilton, 1988; Hoisch and

Simpson, 1993; this study), supports that crystal-plastic deformation was active in both quartz and calc-mylonite during ca. 12-7 Ma BCD slip.

## 3. Methods

### 3.1. Field and analytical methods

The BCD fault core was identified, measured, described, and sampled along a 15 km surface trace (Fig. 1 and Table 1). Meso-scale structures (e.g., fault planes, foliations, shear planes, fold axes, stretching lineations, slickenlines, separation magnitudes) were measured in the field and in cut hand samples. Fault core samples were epoxied, cut, and selected for oriented polished thin sections. Oriented thin sections were cut 1) parallel to mylonitic stretching lineations and perpendicular to C-planes in mylonite samples, or 2) parallel to slickenlines and perpendicular to Y-shears in cataclasite and foliated gouge samples.

We utilize S–C–C' terminology (Berthé et al., 1979; Lister and Snoke, 1984; Vauchez, 1987; Shimamoto, 1989) for descriptions of ductile fabrics within mylonite and P–Y-R1 terminology (Riedel, 1929; Tchalenko, 1970; Logan, 1979; Petit, 1987; Volpe et al., 2022) for description of the brittle fabrics within cataclasite and gouge.

For readers unfamiliar with these terms, S–C–C' fabrics form through the intersection of foliations and shear bands during metamorphism, cataclasis, and dynamic recrystallization. The S-foliations (for schistosity) are typically defined by oriented elongate mineral grains. They form parallel to the direction of maximum elongation (Ramsay and Graham, 1970; Shimamoto, 1989) and rotate during shear strain. The C-surfaces (French cisaillement for shear) are micro shear bands and represent planes across which there has been horizontal motion (Berthé et al., 1979). The C'-surfaces are shear bands (also referred to as extensional crenulation cleavage) that develop after significant shear strain has accumulated (Platt and Vissers, 1980; Simpson and Schmid, 1983; Vauchez, 1987). They may cross-cut or anastomose with existing S–C fabrics and are typically inclined 15–20° in the direction of motion relative to the original C-surfaces. Movement along C'-surfaces requires net extension in the direction parallel to earlier formed C-surfaces (Platt and Vissers, 1980).

Brittle mineral alignments and planar fabrics are described with P–Y-R1 terminology, which are essentially the brittle counterparts of S–C–C' planes, respectively (Shimamoto, 1989). P-shears are the brittle analogues to ductile S-foliations. They are characterized by preferred orientation of mineral grains (often clays) that probably align with long axes parallel to the direction of maximum elongation within the shear zone (Haines et al., 2013). Y-shears are the brittle analogues to ductile S-foliations and represent simple shear planes subparallel to the shear zone boundary. R1-shears, or Riedel shears (Riedel, 1929) are analogous to C'-planes in that they form at a gently inclined angle (15–30°) to Y-shears, can crosscut or anastomose with existing P–Y shears, and accommodate net extension parallel to the shear zone boundary. The

**Table 1**
Fault rock lithotypes, gouge zone phases, and reconstructed T-t conditions for study sites along the BCD.

| Location | Lat | Lon | fault rocks present at location | | | | | | | | | Reconstructed T of footwall adjacent to sample locations (Lutz et al., 2021) | | | |
|---|---|---|---|---|---|---|---|---|---|---|---|---|---|---|---|
| | | | foliated gouge | | | | structureless gouge | brec | qtz-cat | MPC | my | 12 Ma | 10 Ma | 8 Ma | 0 Ma |
| | | | qtz | cal | dol | illite | | | | | | | | | |
| BCD-08 | 36.744463 | −116.969103 | 1 | 2 | 3 | 4 | x | x | x | x | x | 350 °C | 330 °C | 240 °C | 55 °C |
| BCD-07 | 36.735861 | −116.914969 | 1 | | | 2 | | x | | | | 300 °C | 260 °C | 175 °C | 50 °C |
| BCD-06 | 36.726018 | −116.899278 | 1 | 2 | 3 | 4 | | x | | | x | 280 °C | 245 °C | 160 °C | 45 °C |
| BCD-04 | 36.718541 | −116.891658 | Not observed | | | | | x | | | x | 270 °C | 230 °C | 150 °C | 45 °C |
| BCD-03 | 36.714095 | −116.861841 | Observed but not analyzed | | | | x | x | | | | 260 °C | 220 °C | 140 °C | 35 °C |
| BCD-02 | 36.698340 | −116.8283332 | 1 | 3 | 4 | 2 | x | x | | | x | 250 °C | 200 °C | 130 °C | 35 °C |
| BCD-01 | 36.696901 | −116.824764 | 1 | | | 2 | | | x | | | 240 °C | 190 °C | 125 °C | 30 °C |

1 … 4: phase presence in order of decreasing abundance; blank cell indicates phase or rock type not present at study location qtz: quartz, cal: calcite, dol: dolomite, brec: breccia, cat: cataclasite, MPC: mixed phase cataclasite, my: mylonite.

reader is referred to Volpe et al. (2022) for a recent exhaustive review and analysis of these microstructural discontinuities.

### 3.1.1. XRD

Clay-rich gouge, cataclasite, and adjacent wall rock samples were collected for X-ray diffraction (XRD) analysis to determine mineralogy. Several samples spanning vertical thicknesses of ~1 m were collected from the composite gouge zones (Fig. 1D). Samples were crushed and powdered with a mortar and pestle and placed into machined aluminum discs. These were scanned for 10 min over 90° 2$\theta$ with a Panalytical X'Pert Pro Diffractometer at the New Mexico Bureau of Geology and Mineral Resources. XRD spectra were matched with mineral species using the PanAnalytical program HighScorePlus. The program identifies peaks and troughs within the spectra and compares them to an established suite of standards. (https://www.malvernpanalytical.com/en /products/category/software/x-ray-diffraction-software/highscore-w ith-plus-option). Mineral phases that constitute less than 1–2% of the rock (e.g., oxides, sulfides) were not identified by XRD. We did not attempt exhaustive methods to separate the different forms of illite and recognize that longer scans may allow more precise determination of gouge compositions (e.g., Haines and van der Pluijm, 2012).

Mineralogy determined from the XRD spectra was used to assign friction (static and rate-state) to the fault for modeling, identify fault rock protoliths, and estimate contributions from the hanging wall and footwall. Frictional properties were assigned by comparison to thermally controlled laboratory experiments performed on rocks with similar compositions (e.g., den Hartog et al., 2012b, 2013).

### 3.1.2. Petrographic microscope and microprobe

The microstructure and geochemistry of fault rock samples were analyzed using a petrographic microscope and a scanning electron microscope (SEM). Microstructural relationships and dynamically recrystallized grains were observed and measured using a Keyence 3-D Digital Microscopy System at the U.S. Geological Survey Geosciences and Environmental Change Science Center. The average dynamically recrystallized grain sizes of calcite and quartz within calc-mylonite were used to estimate differential flow stress through calibrated piezometers (e.g., Stipp and Tullis, 2003; Cross et al., 2017; Heilbronner and Kilian, 2017; Platt and De Bresser, 2017; Platt, 2023). The size and structural configuration of clays within foliated gouge were observed with the SEM. The contact between wall rock mylonite and brittle cataclasite was imaged for textural characteristics and mapped compositionally using a Cameca SX-100 electron microprobe at the New Mexico Bureau of Geology and Mineral Resources.

### 3.2. Modeling methods

Exposures along the fault trace were reconstructed to their paleodepths and temperatures through time using the cross-section reconstructions and thermo-kinematic models of Lutz et al. (2021). The fault core was generally assumed to translate with the footwall, with upward conductive heat flow sufficiently rapid that fault core temperature tracks modeled temperature of the upper footwall. This assumption is consistent with models that invoke progressive incision as a mechanism to form and sustain throughgoing low-angle detachment faults (Lister and Davis, 1989; Forster and Lister, 1999; Osmundsen and Ebbing, 2008; Long and Walker, 2015; Wiest et al., 2020; Davis et al., 2023; Gresseth et al., 2023). The modeled thermal histories of individual exposure sites were then used to infer the timing of formation of various fault rocks.

Simple 2D static stress models were developed to approximate shear stress at different depths along the initial BCD (ca. 12 Ma). Principal stress magnitudes were treated as pressure gradients (MPa/km) using the stress module built into the Move software (Petroleum Experts LTD., 2024). We used a vertical maximum principal stress ($\sigma_1$) given by a lithostatic pressure gradient (assuming rock density $\rho$ = 2600 g cm$^{-3}$;

26 MPa/km) and a horizontal minimum principal stress ($\sigma_3$) given by a 12 MPa/km pressure gradient. The maximum and minimum principal stresses ($\sigma_1$ and $\sigma_3$) were assumed to lie within the cross-section plane of Lutz et al. (2021). These assumptions are supported by fault kinematic data and by extension-parallel folds with axes sub-parallel to the cross-section (Fig. 1A) (Hoisch and Simpson, 1993; Wright and Troxel, 1993; this study). We also tested configurations with a non-vertical maximum principal stress ($\sigma_1$) near the brittle-ductile transition based on microstructural observations (see below) and based on the assumption that $\sigma_1$ lies at 45° to the boundaries of ductile shear zones (e.g., Selverstone et al., 2012; Axen, 2020).

Normal and shear stress were calculated at various depths using the prescribed inputs for $\sigma_1$, $\sigma_3$, and fault dip magnitudes from Lutz et al. (2021):

$$\sigma_n = \tfrac{1}{2}\left[\sigma_1 + \sigma_3\right] + \tfrac{1}{2}\left[\sigma_1 - \sigma_3\right]\cos 2\theta$$

$$\sigma_s = \tfrac{1}{2}\left[\sigma_1 - \sigma_3\right]\sin 2\theta$$

Where $2\theta$ is the angle between $\sigma_1$ and the fault plane of interest. The ratio between shear stress required to induce sliding ($\sigma^*_s$) and normal stress ($\sigma_n$) is given by Amontons' Law (Amontons, 1699; Coulomb, 1785) modified to include the reducing effect of pore fluid pressure on normal stress, and assuming zero fault cohesive strength (Fossen, 2016; Scholz, 2019):

$$\sigma^*_s = \mu_s\left[\sigma_n - P_f\right]$$

$$\lambda = P_f / \sigma_1$$

Where $\mu_s$ is the coefficient of static friction, $P_f$ is the pore fluid pressure, $[\sigma_n - P_f]$ is the effective normal stress ($\sigma^*_n$), plotted on the x-axis of the Mohr diagrams, and $\lambda$ is the ratio of pore fluid pressure to the maximum principal stress. Hydrostatic pore fluid pressure ($P_f$; $\lambda \approx 0.37$) was assumed for the upper crust (depth $\leq 9$ km), and elevated pore fluid pressure ($P_f$ = 100–200 MPa; $\lambda \approx 0.40$–0.67) was tested in deeper models (depth $>9$ km). Best-fit static stress estimates were made by varying the orientation of the stress field from vertical to steeply NW-plunging ($\sigma_1$ plunge from 60 to 90°; e.g., Axen and Selverstone, 1994), coefficient of static friction ($0.38 \leq \mu_s \leq 0.51$), and pore fluid pressure (hydrostatic $< P_f < \sigma_2$). These values are supported by observations on the fault rocks (see section 4) and comparison to laboratory experiments presented below.

## 4. Results

The BCD fault core was studied in detail at seven localities spanning an ~15-km-long NW-SE surface trace (Fig. 1). The measured sections of the fault core reveal that the BCD separates a hanging wall composed of dolostone breccia and illite-rich gouge from a footwall composed of quartzite breccia, calc-mylonite, injection veins of cataclasite, and pelitic schist (Fig. 2). Generally, individual mylonite layers are <1 m-thick, cataclasite veins are 0.1–10 cm-thick, breccia layers are <1-2 m-thick, and gouge zones are 1–10 m-thick (Fig. 2).

The BCD does not appear to have a single, well-defined principal slip surface. Instead, several principal displacement zones are present within the layered fault rocks. The principal slip surface is mostly covered or nonexistent due to distributed shear in clay gouge. Natural exposures were encountered only at a few sites and were elsewhere dug out from under float. The principal slip surface is broadly undulatory at the meter scale but is well-defined stratigraphically. It is possible that the lows correspond to thick patches of fault gouge (e.g., Brodsky et al., 2011), though this relationship was not documented systematically. Where observable, the surface is generally subhorizontal or dips gently NE (10–20°). The contact between quartzite breccia and overlying clay-rich gouge was often jagged and irregular at the cm-scale, possibly due to late distributed gouge flow. We infer that most of the slip was focused on the
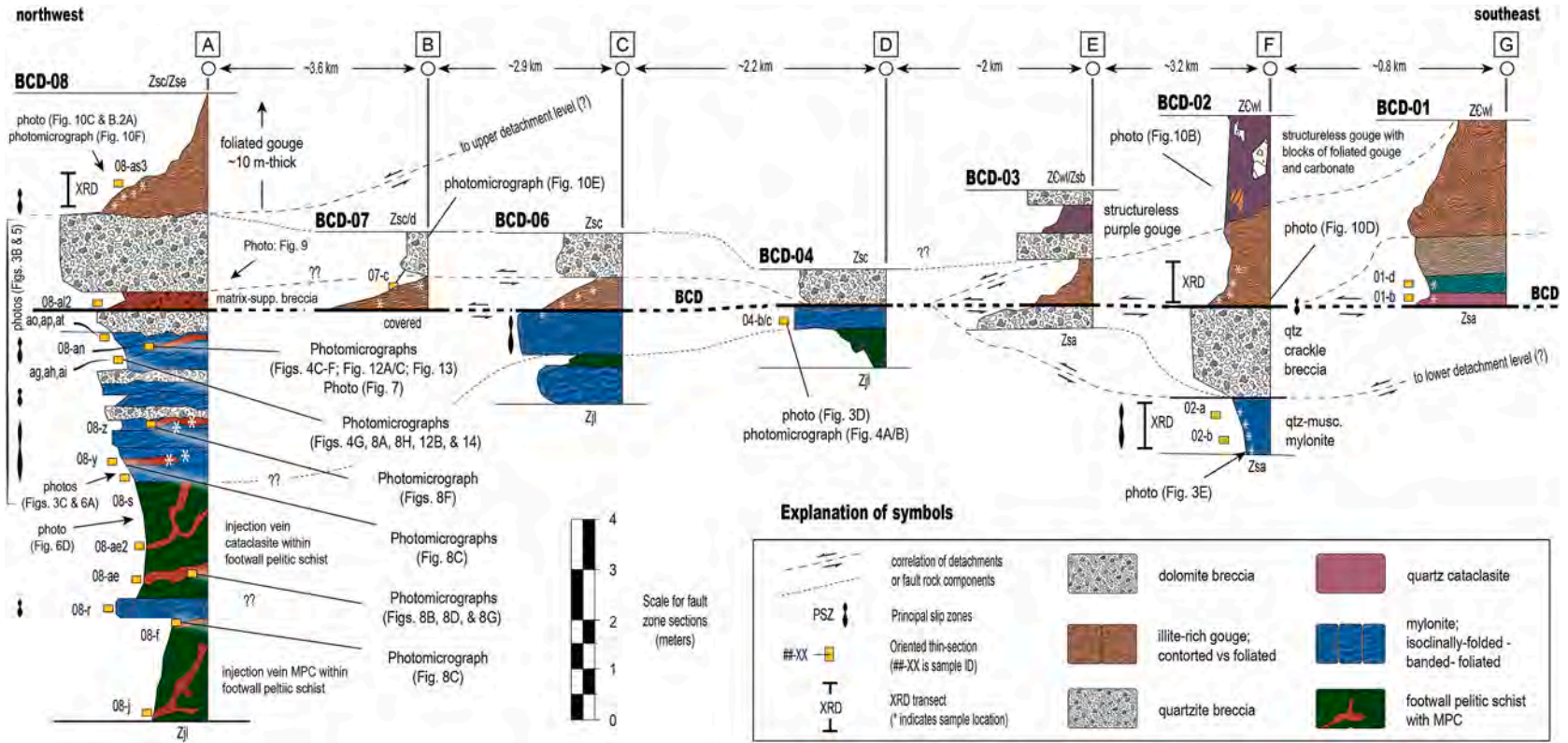
**Fig. 2.** Measured sections showing the thickness and nature of the BCD fault core from NW (A) to SE (G). The study location number is placed on the bar above the section. The BCD is interpreted as the thick bold black line on which the sections are hung. The locations of field photos, oriented thin sections, photomicrographs, and XRD sample transects are noted within the sections. The thicknesses of cataclasite injections in A are exaggerated. The map units in the hanging wall and footwall are described in Fig. 1. The contacts between fault rocks and undeformed hanging wall strata are everywhere covered. ZЄwl, ZЄwm, ZЄwu: lower, middle, and upper members of the Wood Canyon Formation. Zjl: lower member of the Johnnie Formation. Zsa … Zse: A through E members of the Stirling Quartzite.

calc-mylonite layers and within thick hanging wall gouge zones (Fig. 2).

The layered nature of the fault rocks along the BCD is consistent with the fault traversing a metasedimentary to sedimentary sequence composed of pelitic schist (Zjl), carbonate (Zjl & ZЄws), quartzite (Zs), and siltstone/shale (ZЄws) (Figs. 1 and 2). The alternating sequences of quartz- and calc-mylonite and quartz breccia in the BCD footwall reflect the fault cutting through pelitic schist, carbonate, and quartzite beds, respectively. The gouge zones, interpreted to be derived primarily from the hanging wall (see section 4.4), are primarily the product of the fault cutting through siltstone and dolostone within the upper crust (Fig. 1D). The outcrop structure, microstructure, and composition of each fault rock litho-type are detailed in the following subsections.

### 4.1. Mylonite

Mylonite was observed and described in the BCD footwall at study locations BCD-08, -06, −04, and −02 (Fig. 2). The thick section of layered calc-mylonite and quartzite breccia at BCD-08 is the most complete and representative footwall section. Thin mylonite layers at BCD-06 and BCD-04 likely correlate to the BCD-08 location, though the footwall of the fault core at BCD-07 was covered (Fig. 2B). The quartz-muscovite mylonite at BCD-02 coincides with a schistose interval in the A member of the Stirling Quartzite where it intersects the BCD.

Both outcrop and microstructural fabrics within mylonite record top-NW shear consistent with the BCD gouge zones and regional BCD-kinematics. Top-NW shear fabrics include stretching lineations along C-planes with apparent separation (Fig. 3C and D), S–C–C′ planes (Fig. 3E and 4, and C1), mesoscale asymmetric folds (Fig. 3E), asymmetric porphryoclasts (Fig. 4A and C.1), and overprinting brittle shears (Fig. C1). The maximum eigenvector of stretching lineations at the BCD-08 location plunges gently NW (10°/294°), which is subparallel to that from brittle grooves and slickenlines across all BCD study locations (10°/300°) and the mean vector of top-NW transport estimated by Hoisch and Simpson (1993) (toward 299° ± 12°; Fig. 4I).

Mylonite layers are massive, banded or isoclinally folded (Figs. 2 and 3). Mylonite layers at BCD-08 and BCD-04 contain very fine calcite matrix, sub-mm-thick micaceous intervals, sub-mm- to cm-thick sigmoidal-to slightly deltoidal mantled quartz porphryoclasts (Figs. 2, 3 B-3D, and C.1), and euhedral to subhedral pyrite and hematite (Fig. C2). Brittle fracturing of quartz was contemporaneous with crystal-plastic flow of the calcite, based on outcrop observations of quartz ribbons at BCD-08 (Fig. 3C) and microstructure of quartz sigmoidal porphyroclasts at BCD-04 (Fig. 4A). Calcite that fills tensile and shear veins cutting quartz porphyroclasts and mylonite layers in whole is dynamically recrystallized (Fig. 4A and F).

Calc-mylonite layers exhibit SGR-BLG microstructure in places where the microstructure is organized and not disrupted by brittle microfaulting (Fig. 4C). Measured calcite grains from these areas are on



**Fig. 3.** Field photos of BCD exposures. A) Panoramic view looking SE at the Boundary Canyon detachment (BCD) near the structurally deepest BCD-08 location. B) Outcrop of the main fault core and footwall fault rocks of the lower Johnnie Formation (Zjl) at BCD-08. Outcrop shows layered mixed phase cataclasite (MPC), quartzite breccia, and mylonite. View to the NNE. C) Very fine lineated calc-mylonite from unit Zjl at BCD-08 with inset showing cut sample BCD-08s. View to the NNW. Arrow is stretching lineation that roughly parallels intersection lineations. D) Very fine lineated calc-mylonite at BCD-04 (Zjl). View to the NNE. Arrow is stretching lineation. Sample is BCD-04c. E) Asymmetric z-fold in quartz muscovite mylonite within the A member of the Stirling Quartzite at BCD-02. View to the S. Tsa: Miocene sedimentary and volcanic rocks in BCD hanging wall. Zsc/e: C and E members of the Stirling Quartzite.
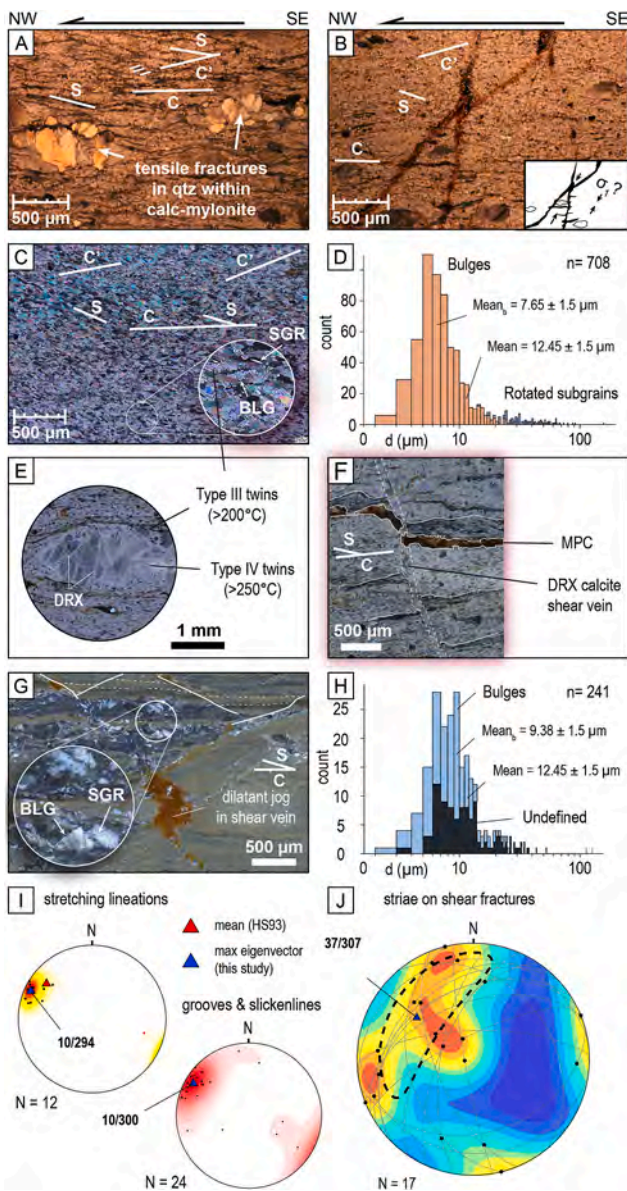
**Fig. 4.** Key microstructural relationships in mylonite samples from the BCD footwall. A) XPL photomicrograph of sample BCD-04 A showing mixed brittle-ductile fabrics. Note anastomosing foliations and shear bands in calcite matrix and tensile fractures in quartz porphyroclasts which are in turn filled with dynamically recrystallized calcite. B) XPL photomicrograph of sample BCD-04 A showing possible conjugate fractures and inferred maximum stress plunge in the section plane relative to C-plane. C) XPL photomicrograph of sample BCD-08AN immediately below the BCD showing organized SGR-BLG microstructure. D) Histogram showing the distribution of measured grains from calc-mylonite samples. E) XPL photomicrograph of sample BCD-08AN showing a large calcite crystal with type III and type IV twinning. F) XPL photomicrograph of sample BCD-08AN showing a shear vein that offsets mixed-phase cataclasite and is in turn dynamically recrystallized. G) XPL photomicrograph showing microfaulting and BLG-SGR microstructure of a quartz ribbon within the brittle-ductile sample BCD-08AI. H) Histogram showing the distribution of measured dynamically recrystallized quartz grains in calc-mylonite samples. I) Lower hemisphere equal area spherical projections (stereonets) of stretching lineations (top left) and brittle grooves and slickenlines (bottom right). The maximum eigenvectors are shown and compared to the mean transport interpreted from Hoisch and Simpson (1993). J) Lower hemisphere equal area spherical projection of convincing striae on shear fractures showing the maximum eigenvector and a cone of 95% confidence (dashed ellipse). BLG: bulging. d: diameter. SGR: subgrain rotation. DRX: dynamically recrystallized. HS 1993: Hoisch and Simpson (1993). MPC: mixed phase cataclasite. Qtz: quartz.

average $12.45 \pm 1.5$ μm in their long dimension. Bulges average $7.65 \pm 1.5$ μm (Fig. 4D). The mean of the bulge measurements suggests crystal-plastic flow stresses of $110 \pm 20$ MPa using the Platt and De Bresser (2017) piezometer or $125 \pm 15$ MPa using the $10°$ subgrain piezometer of Platt (2023). The mean of all grains suggests flow stress of 70–80 MPa. We note that these are likely minimum estimates because there was probably significant annealing following grain size reduction. Furthermore, there are abundant grains with diameters of 4–5 μm, which would suggest higher flow stresses (~170 MPa).

Calcite crystals within the bulk mylonite layering and within veins exhibit thick, curved twins and completely twinned crystals consistent with type III twinning (Burkhard, 1993) (Fig. 4E). This twinning pattern indicates temperatures >200 °C (Burkhard, 1993; Ferrill et al., 2004). Type II and type IV twins are present but less common in the samples. Fig. 4E shows a fairly large calcite crystal within calc-mylonite that exhibits type IV and type III twinning. Some of the twins are thick, patchy and/or dynamically recrystallized such that they resemble the surrounding fine-grained calc-mylonite matrix. These type IV twins likely formed at temperatures >250 °C (Burkhard, 1993; Ferrill et al., 2004).

Dynamically recrystallized grains in quartz ribbons and porphyroclasts measure on average $12.45 \pm 1.5$ μm, with the bulges averaging $9.38 \pm 1.5$ μm (Fig. 4G and H). This bulge value is consistent with the ~10 μm approximation for initially reduced grain size of Hoisch and Simpson (1993). The $9.38 \pm 1.5$ μm grain size yields differential flow stress of $120 \pm 15$ MPa using the Heilbronner and Kilian (2017) piezometer, which was calibrated using general shear. Using the mean grain size of $12.45 \pm 1.5$ μm, the same piezometer yields differential flow stress of $110 \pm 10$ MPa.

### 4.2. Cataclasite

Cataclasite bands and veins are preserved within the inter-layered sequence of mylonite and quartzite breccia at the structurally deepest fault exposure, BCD-08 (Fig. 2A and 3B). The cataclasite exhibits a distinct red-brown staining from the presence of iron oxide. It localized systematically near strength contrasts within the layered fault rocks of the BCD footwall. That is, cm-thick cataclasite bands and veins proliferate between the quartzite breccia and calc-mylonite layers (Fig. 5), and mm-thick cataclasite bands and veinlets formed between quartz- and matrix-rich intervals of the mylonite layers (Fig. 5D, 6B and 6C). Within quartzite breccia and quartz ribbons, the cataclasite occupies mm-thick tensile cracks and veins (Fig. 5A and E). Within the mylonite layers, the cataclasite occupies mm-to cm-thick bands and veins sub-parallel to preexisting S–C–C' planes (Figs. 5 and 6).

The cataclasite is clearly injected into the footwall calc-mylonite (Fig. 5B, 6A and 6D) and quartzite breccia (Fig. 5E). The injection veins are 0.1–2 cm-thick and extend for up to 30 cm in length (Fig. 6D). The injection veins appear to have accommodated 0.1–5 cm of shear and dilation. Contacts between the injection veins and quartzose wall rocks are cuspate and lobate (e.g., Fig. 5B, D, and 5E), whereas contacts with matrix of mylonitic wall rock are more undulatory (Figs. 5D, 6B and 6D).

Injection veins of cataclasite are composed of a mixture of illite, quartz and calcite in proportion similar to wall rock mylonite (Fig. 6E). This indicates in-situ mechanical derivation from the calc-mylonite and quartzite breccia layers. We hereafter refer to the cataclasite as mixed phase cataclasite (MPC).

We observed one late stage (?) low-angle MPC band with small offset (~4 cm), which may represent a proxy for the larger BCD (Fig. 7). The band cuts relatively steeply through a quartzite breccia layer and gently (~25°) through the calc-mylonite. Tensile cracks and veins within the footwall of the MPC band are filled with injected MPC. The entire area within 0.5–1 m from the inclined MPC band is highly brecciated and altered (Fig. 7A).

Outcrop and hand sample patterns of MPC are reflected at the microscopic scale. The MPC zones are localized systematically at

**Fig. 5.** Outcrop and cut sample photos showing macro-to meso-scale relationships between mixed-phase cataclasite (MPC) and wall-rocks. The MPC zones systematically formed between weak calc-mylonite and strong quartzite breccia layers (A, C, D). B) Cut sample of injection vein of MPC with jagged wall-rock contact characterized by cusps. D) Characteristic attitude of MPC zone subparallel to mylonitic foliations and shear bands. Note injection of MPC into thin, subvertical cracks within the overlying quartz-rich band E) Cut sample showing MPC filling tensile cracks within a quartz ribbon of the calc-mylonite. Note the cuspate-lobate nature of the contact between the MPC and the underlying calc-mylonite with quartz ribbons.
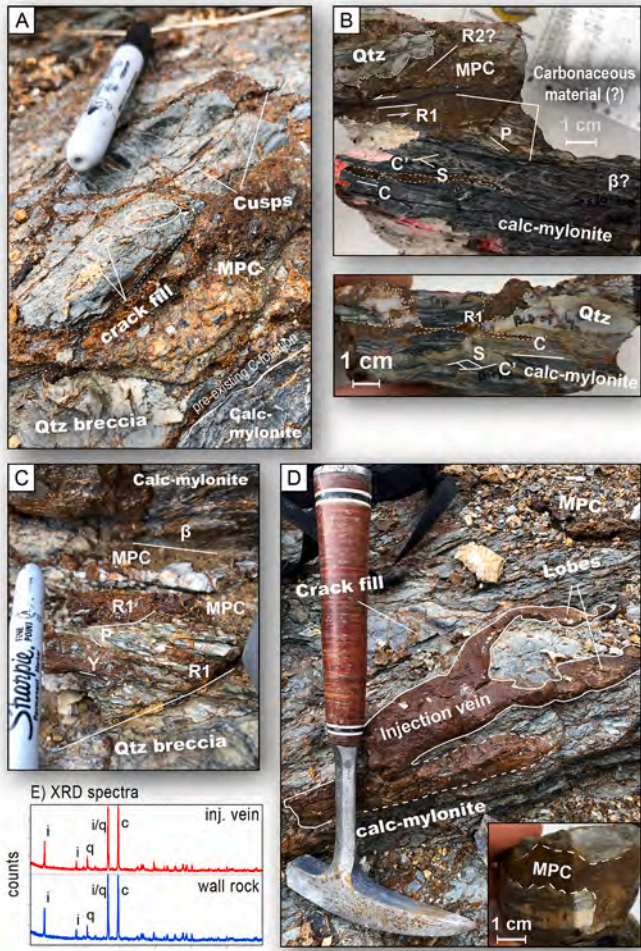
**Fig. 6.** Outcrop and cut sample photos showing characteristic relationships between mixed-phase cataclasite zones (MPC) and wall-rocks. A) MPC injection emplaced subparallel to mylonitic C-plane and injected into tensile cracks and shear fractures. Note the cusp-like contacts with wall rock. View to the NW. B) Cut samples of MPCs emplaced along R1 fractures that reactivate C′-planes in footwall mylonite. In bottom cut sample photo, MPC in quartz tensile cracks is confined to the zone above the bounding R1, which appears to have localized preferentially within the quartz-rich band of calc-mylonite country rock. C) Meso-scale MPC bands emplaced at contact between quartzite breccia (below) and calc-mylonite (above). View to the NNE. D) Injection vein of MPC with angular fragments of wall-rock mylonite arranged in a granular flow fabric along bounding surfaces. View to the N. Inset shows cm of dilation around injection vein from cut sample. E) XRD spectra showing similarity in crystallinity between MPC (in D) and wall-rock sample. i: Illite. q: quartz. c: calcite.

preexisting S–C–C' planes within the mylonite and accommodate mm-scale offsets. We therefore interpret that they represent P, Y, and R1 shears. The R1 shears preserve the largest apparent separation and formed preferentially at strength contrasts within the mylonite (i.e., contacts between quartz ribbons or porphyroclasts and calcite- or mica-rich matrix; Fig. 8A).

The cuspate and lobate contacts between the MPC and wall rocks are prevalent at the microscopic scale as well (Fig. 8B). Clasts entrained within the MPC matrix are both elongate pieces of mylonite wall rock (Fig. 8B), fragmental quartz survivor grains (Fig. 8E and G), and mica (Fig. 8D). The entrained clasts appear to be plucked from the MPC wall rocks and have shape-preferred orientations. The elongate pieces of wall rock mylonite align parallel to the MPC margins (Fig. 8B and C), the quartz survivor grains are aligned to R1 shears and subparallel micro-faults (Fig. 8D and E), and the mica grains show an array of orientations and bent geometries (Fig. 8D).
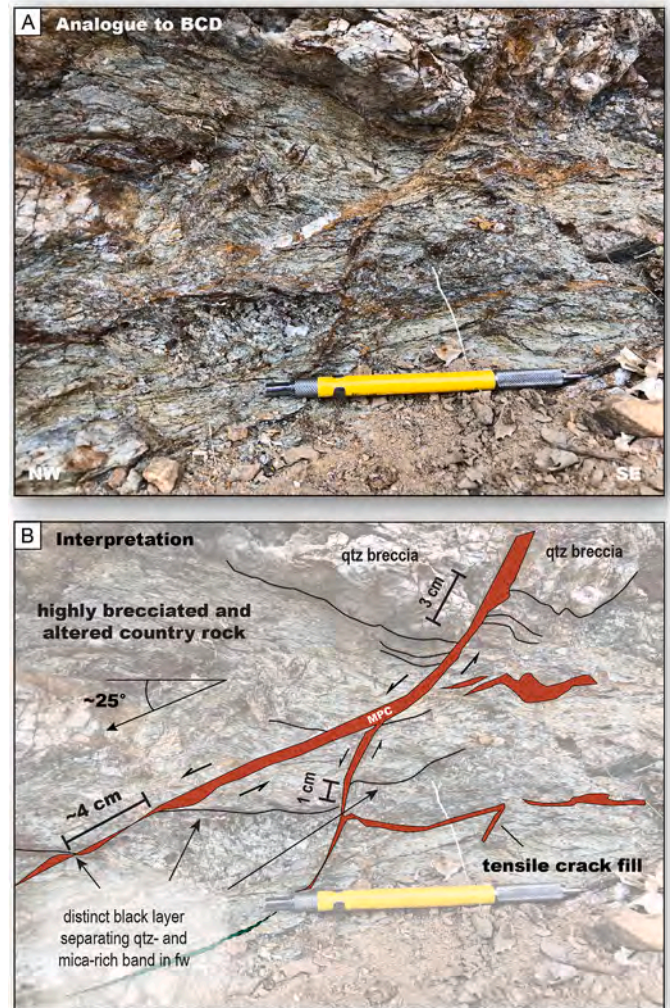


**Fig. 7.** Outcrop photo showing meso-scale faulting analogous to the Boundary Canyon detachment (BCD). Small normal sense separation (3–4 cm) is measured from offset contact between quartzite breccia and mylonite layers. The fault is occupied by very fine MPC with characteristic iron-oxide staining. The small proxy fault dips ~58° through the quartzite breccia and ~25° through the mylonite. Qtz: quartz or quartzite. MPC: mixed phase cataclasite.

The texture and geochemistry of an MPC-wall rock contact are depicted in electron microprobe images (Fig. 8G). The contact characterized by predominately K-, Ca-, and Si-rich mineral phases interpreted as illite, crystalline calcite, and quartz, respectively. Fe-rich phases are interpreted as subhedral to euhedral hematite in the wall rock as disseminated iron oxide within the MPC matrix. The hematite present along shear bands and within MPC replaces pyrite within calc-mylonite layers (Fig. C1), presumably via dissolution and oxidation during embrittlement and meteoric water influx (see section 5.2). The adjacent MPC is a mixture of very fine (<5–40 μm) quartz and calcite grains in a finer matrix rich in iron. The very comminuted quartz grains were most likely derived from an adjacent larger grain (~200 μm) located along the MPC contact, possibly the generation surface. Crushing and comminution of quartz and calcite during MPC formation is reflected also in the preservation of ultracataclasite along the margins of MPC zones (Fig. 8F).
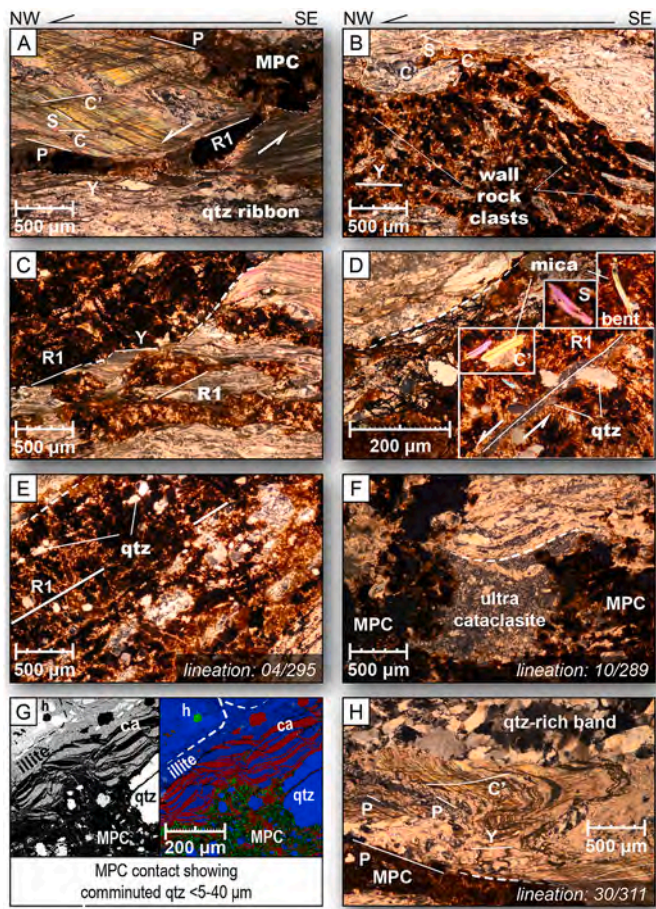
**Fig. 8.** XPL photomicrographs (A-F; H) and elemental maps (G) of mixed phase cataclasite (MPC) zones and contacts with wall rocks inferred to be generation surfaces generation surfaces (white dashed lines). A) Brittle reactivation of C′-type mylonite at a quartz ribbon. Sample: BCD-08ai. Lineation: 30/311. B) Undulating contact between MPC and wall-rock with small cusps and lobes. Wall rock clasts are aligned parallel to the margin, indicative of laminar fluidized flow. Sample: BCD-08ae3. Lineation: 04/295. C) MPC aligned to R1 and Y shears that reactivate C′-type mylonite. Sample: BCD-08 y. Lineation: 11/298. D) R1-aligned contact between MPC and wall rock and S–C′-oriented mica grains within MPC. Sample: BCD-08ae3. Lineation: 10/289. E) R1-alignment of generation surface and quartz survivor clasts within the MPC. Sample: BCD-08f. Lineation: 04/295. F) Preservation of quartz ultra-to mesocataclasite along inferred MPC generation surface. Sample: BCD-08z. Lineation: 10/289. G) Backscattered electron image (left) and elemental map (right) of contact between MPC and wall in sample BCD-08ae3. Individual phases are labeled. Colors in elemental map: Green (Fe), Red (Ca), Purple (K), Blue (Si). These are interpreted as hematite (h), calcite (ca), illite, and quartz (qtz), respectively in the image. H) Y- and P-shear aligned MPC zone. Sample: BCD-08ai. Lineation: 30/311. (For interpretation of the references to color in this figure legend, the reader is referred to the Web version of this article.)

## 4.3. Breccia

Quartzite and/or dolostone breccia were observed in the BCD fault zones at most locations (Fig. 2 and Table 1). Quartzite breccia layers predominate where the A member of the Stirling Quartzite or the lower Johnnie Formation comprise the footwall. Dolostone breccia are present where the "C" member of the Stirling Quartzite or the lower Wood Canyon Formation comprise the hanging wall. White quartzite breccia is interlayered with footwall mylonite at BCD-08 (Fig. 2A). The breccia is generally chaotic to mosaic and matrix supported.

Chaotic, matrix supported breccia layers are interpreted to mark the immediate hanging wall of the BCD at BCD-08 (Fig. 9). At this locality, there is an erosionally resistant ~1–1.5 m-thick layer of orange-brown,
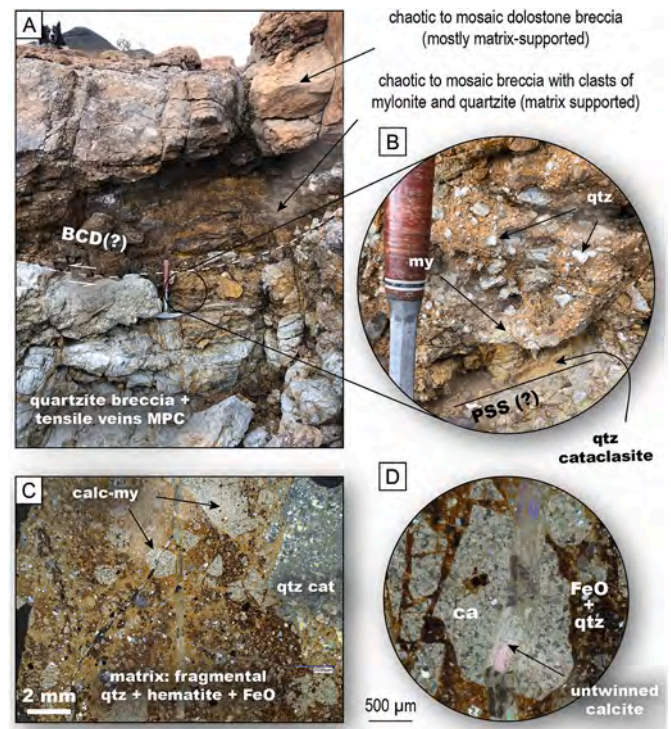


**Fig. 9.** Field photos (A/B) and photomicrographs (C/D) showing the structure of breccia layers at the BCD-08 locality. A) Breccia layers separating quartzite breccia and mylonite (footwall) from thick foliated illite-rich gouge (hanging wall). B) matrix-supported chaotic breccia with clasts of quartzite (qtz) and mylonite (my). A principal slip surface (PSS) may be present at the base, overlain by quartz cataclasite. C) Photomicrograph of sample BCD-08al2 showing structure and clast composition of the matrix supported, chaotic breccia. Clasts are calc-mylonite, quartz cataclasite, fragmental quartz (qtz), and hematite (fragmental and disseminated FeO). D) photomicrograph showing tensile veins cutting breccia matrix and clasts filled with untwinned calcite. Ca: calcite.

dolostone mosaic-to chaotic matrix supported breccia. This breccia overlies a layer of erosionally recessive ~0.5-1 m-thick orange-red-black chaotic matrix supported breccia with clasts of predominately mylonite and quartzite, and quartz cataclasite. These breccia layers separate the layered cataclasite-mylonite sequence below from a thick (>10 m) section of foliated illite gouge above (Figs. 9 and 3B, and B2A). The matrix of the lower breccia resembles MPC in its orange-brown-red color, which is presumed to be iron oxide (amorphous hematite). The matrix contains fragmental quartz and subhedral to euhedral hematite (Fig. 9C) and is crosscut by pervasive tensile veins of calcite lacking any twinning (Fig. 9D). Aside from these rudimentary observations, the breccia layers were not studied in detail.

## 4.4. Clay-rich gouge

Clay-rich gouge is present at all study sites except BCD-04. Gouge exposed along the BCD is predominantly illite-rich, incohesive, very fine grained, and foliated (Fig. 10C). Incohesive, pulverized, structureless gouge (Fig. 10B) and cohesive, contorted lithon-rich foliated gouge are also present (Fig. 10E and B.1).

Foliated illite-rich gouge zones range in thickness from ~0.5 to >10 m, being thickest at the structurally deepest, northwestern exposure (>10 m; BCD-08; Fig. B2A) and in the southeastern-most study sites (3–10 m; BCD-01 and BCD-02) (Fig. 2). XRD and microprobe scans show that the gouge is generally an illite-quartz-carbonate mixture, with variable portions of each (Table 1). Gouge samples from BCD-01, BCD-02, and BCD-07 contain a high fraction of illite (~25–75%), whereas

**Fig. 10.** Field photos (A–D) and photomicrographs (E and F) focused on BCD gouge zones. A) View to the SE of hanging wall normal faults soling into the BCD and pulverized structureless gouge near the intersection. B) Pulverized structureless gouge with randomly arranged clasts of wall rock and foliated clay gouge. C) Hand sample BCD-08-as3 recovered from foliated clay gouge zone. D) Crude, abrasive wear grooves on breccia at gouge base at BCD-02. View to the NW. Attitudes: 15°/302° ± 10. E) Microlithons in foliated gouge sample BCD-07c showing top-NW shear. F) Photomicrograph of sample BCD-08as3 showing brittle fractures that are predominately anastomosed with some distinct R1. ZƐw: Wood Canyon Formation. Zs: Stirling Quartzite.

gouge samples from BCD-06 and BCD-08 have more quartz and carbonate. The illite-rich matrix supports minor fragmental quartz and calcite grains with angular, fractured edges (Fig. B2).

Outcrop and microstructural observations confirm that the foliated illite gouge zones are kinematically related to BCD-slip. First, the gouge zones consistently occupy the immediate hanging wall of the BCD (Fig. 3A and 10 A, B.2, and B.3). Slickenlines and fault grooves were measured on a fault surface at the contact between the gouge and an underlying quartzite breccia (Fig. 10D and B.4). These plunge sub-parallel to the regional heave direction of the BCD and to ductile fabrics measured in mylonite layers (Fig. 4I) (Hoisch and Simpson, 1993; Lutz et al., 2021). Asymmetric structures within the gouge also show top-NW shear consistent with BCD-kinematics. Hand-sample and oriented sections reveal cm-scale deltoidal lithons and mm-scale sigmoidal to deltoidal porphryoclasts (Fig. 10E and B.1).

Illite-rich gouge zones accommodated predominately stable sliding and high shear strain. The anastomosed Y, P, and R1 shears in foliated illite gouge samples indicate high strains ($\gamma > 10$) (Tchalenko, 1970; Petit, 1987; Haines et al., 2013). Several samples exhibit R1 shear angles that are very low (<15°) relative to the Y-shear planes (Fig. 10F), consistent with stable sliding (Moore et al., 1989) and very high shear strain (Haines et al., 2013). Higher angle R1 shears (15°–30°) relative to the Y-shear plane are common in strain haloes around rigid porphyroclasts (Fig. 10E). These high-angle R1 shears suggest lower shear strain (Haines et al., 2013) at BCD-07, where the gouge zone is very thin (~1 m), than at BCD-08, where gouge zone is very thick (>10 m).

Gouge layers with random fabric are present in several locations

(Fig. 10A and B, and B3D). The purplish structureless gouge at BCD-02 and BCD-03 exhibits a pulverized texture and locally contains blocks of wall rock carbonate and foliated illite-rich gouge (Fig. 2F and 10B). Pulverization and presence of clasts of foliated gouge have been attributed to coseismic fault slip, possibly during dynamic rupture propagation (Rowe and Griffith, 2015; Axen et al., 2018).

We speculate that the gouge zones were derived mainly from the BCD hanging wall, based on field observations and XRD results. First, the colors of thick, foliated illite-rich gouge sections at BCD-01, BCD-02, and BCD-08 resemble distinct units from the hanging wall. For example, at BCD-02 and BCD-03, gouge sections have distinctive yellowish-orange and purple-black colors that closely resemble interbedded dolostone and siltstone of the Wood Canyon Formation (Fig. 10A and B.3 A; orange dolostone, tan dolostone, black siltstone; Wright and Troxel, 1993). At BCD-08, where the footwall is dominated by calc-mylonite and pelitic schist, the ~10 m-thick orange-tan illite gouge zone resembles hanging wall dolostone, silty carbonate and siltstone in the "C" and "E" members of the Stirling Quartzite (Fig. 3A). We recognize that diagenesis could easily obscure the original colors of the gouge zones and that color is not a definitive property with which to correlate gouge zones to protoliths.

XRD transects through the gouge zones generally support that gouge was derived from the BCD hanging wall. Inferred footwall-derived mineral phases mostly decrease within 10–30 cm up section from the base, and inferred hanging wall-derived phases predominate throughout. Perhaps the best example of this is at BCD-06 (Fig. 11B). The footwall is composed of calc-mylonite, whereas the hanging wall is feldspathic sandstone/siltstone and dolostone breccia of the "C" member
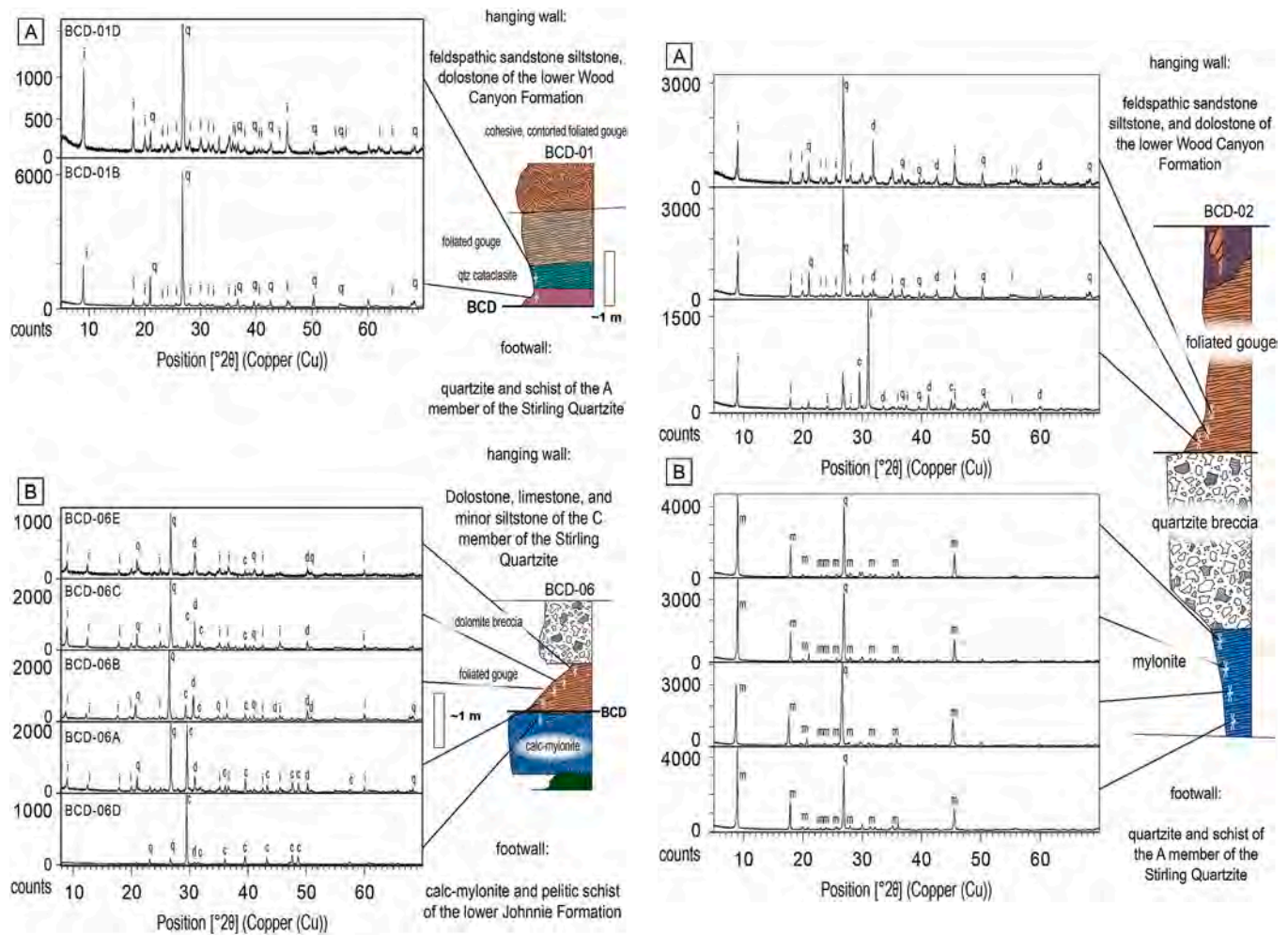
**Fig. 11.** Results of XRD scans from the BCD-01 (A), BCD-06 (B), BCD-02 (C/D), BCD-08 (E), and BCD-07 (F) locations. The dominant undeformed hanging wall and footwall lithologies are described in the text above and below the sections on the right. Minerals corresponding to peaks in XRD spectra are labeled. c: calcite. d: dolomite. i: illite. q: quartz.

of the Stirling Quartzite (Fig. 2C). The basal XRD sample (BCD-06 A) is a mixture of quartz, calcite, and illite (Fig. 11B). The high proportion of calcite suggest high contribution from the footwall calc-mylonite. Samples above the base of the gouge zone are predominately quartz, dolomite, and illite, consistent with increasing contribution from the hanging wall.

At BCD-02, elevated proportions of illite and dolomite ~10 cm up-section from the gouge zone base (Fig. 11C) suggest increased contribution of feldspathic sandstone, siltstone, and dolostone of the lower Wood Canyon Formation, which comprises the immediate hanging wall. At BCD-08, elevated proportions of dolomite 60 cm up-section from the gouge zone base (Fig. 11E) suggest increased contribution of dolostone from the "C" member of the Stirling Quartzite, which comprises the immediate hanging wall (Fig. 3A). Lessened proportions of calcite within ~20 cm of the gouge zone base suggest decreased contribution of calc-mylonite (or possibly carbonate breccia) from the lower Johnnie Formation, which underlies the gouge zone (Fig. 2A). Lastly, we add that high-grade metamorphic minerals, abundant within the footwall of the BCD (e.g., garnet, staurolite) were not identified by XRD or thin section analysis of the gouge zones. One may expect relicts of high-grade minerals if gouges were derived from the footwall, which is dominated by upper amphibolite grade metapelite. We recognize that our XRD transects are somewhat reconnaissance in nature, and that longer scans may reveal other phases as well as help distinguish forms of illite (Haines and

van der Pluijm, 2012), though the data we have generally do support gouge derivation from the hanging wall.

## 5. Interpretations of fault rock genesis

### 5.1. Mylonite: zone of semi-brittle flow

Calc-mylonite of the lower Johnnie Formation formed via crystal-plastic flow near the upper part of the brittle-ductile transition zone along the BCD. The average dynamically recrystallized grain size of bulges in calc-mylonite (7.65 ± 1.5 μm; Fig. 4D) suggests crystal-plastic flow at ~260°-300 °C and 115 ± 25 MPa, based on temperature calibrations (Ebert et al., 2008) and grain size piezometry (Platt and De Bresser, 2017; Platt, 2023). This temperature range is consistent with 1) brittle fracturing of quartz that was contemporaneous with plastic flow of calcite (Fig. 4A and 12A), and 2) the predominance of type III and type IV twinning in calcite (Fig. 4E and 12C). The estimated flow stress is slightly less than that estimated for quartz ribbons and porphyroclasts within calc-mylonite (120 ± 15 MPa), which was calculated using the Heilbronner and Kilian (2017) piezometer.

Pyrite and its oxidized byproducts (hematite) within calc-mylonite suggest redox conditions that evolved with progressive embrittlement. Pyrite is consistently unaltered in calc-mylonite where microstructure is organized and uninterrupted by brittle microfaults (Fig. C2). This
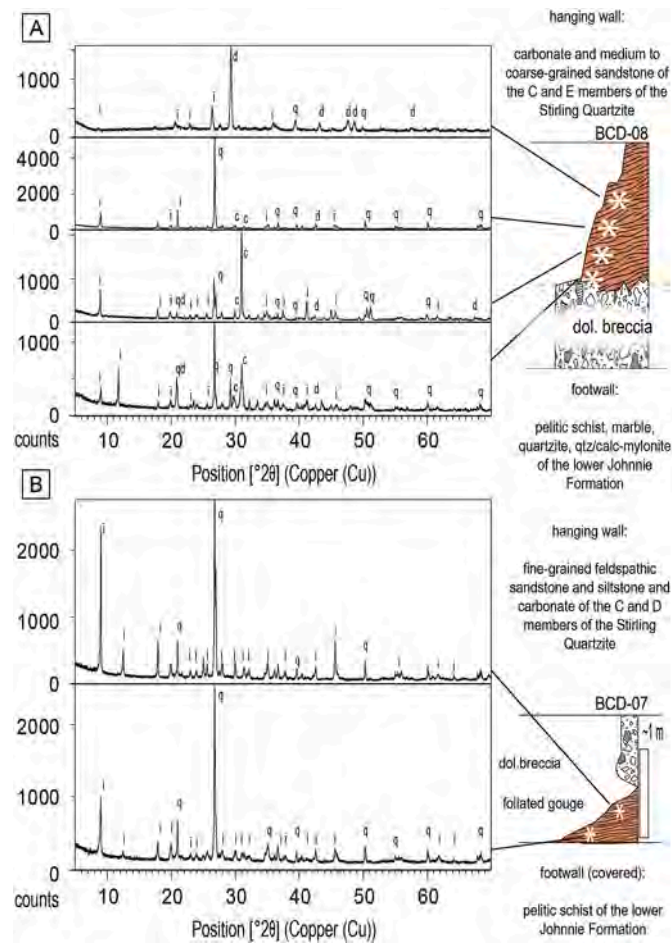
**Fig. 11.** (*continued*).

supports that any fluid present in the plastic shear zone was generally anoxic. However, adjacent to brittle microfaults and within MPC zones pyrite is rimmed or completely replaced by hematite (Fig. C2). This suggests that the embrittlement process oxidized and or thermally decomposed the pyrite (see section 5.2.2 below).

### 5.2. Cataclasite and breccia: earthquake nucleation zone

We interpret that MPC formed via high strain rate coseismic slip along the BCD within the brittle-ductile transition zone and the deep parts of the brittle crust. Formation of MPC via coseismic slip is supported primarily by 1) veins injected into cracks, fractures, and preexisting mylonitic foliations and shear bands (Figs. 5–7; 12 B), 2) the pervasive iron oxide staining in MPC, which could reflect thermal decomposition of carbonates and iron sulfides during coseismic heating (Evans et al., 2014; Rowe and Griffith, 2015), and 3) granular flow textures within MPC (detailed below).

Granular flow can be cataclastic, laminar, and grain-inertial (Rowe and Griffith, 2015). Cataclastic granular flow occurs when clasts or grains slide past one another and fracture internally. Laminar fluidized granular flow occurs when the grains rotate and/or strain internally within a fine-grained flowing matrix. Grain-inertial fluidized flow occurs when grains collide and transfer energy from one to the next (Borradaile, 1981; Paterson, 2013; Rowe and Griffith, 2015). These granular flow mechanisms act together to reduce grain size and weaken a fault. Injection veins and grain-inertial flows are suggested to have coseismic origins (Rowe et al., 2012b; Rowe and Griffith, 2015).

Relics of cataclastic and fluidized granular flow are variably preserved within MPC samples and outcrops. Cataclastic granular flow is recorded by highly angular wall rock clasts (Fig. 6A, D, & 12B), highly angular individual quartz grains (Fig. 8D, E, 8G, and 12E), and quartz grains that are broken and offset in a normal sense along R1 shears (Fig. 8D and 12A). Fluidized granular flow within MPC was both laminar and grain-inertial. Laminar flow is recorded by alignment of the long axes of wall rock clasts to the complex MPC margins (Fig. 8B and D.1) and shape preferred orientations of mica grains within MPC matrix (Fig. 8D).

#### 5.2.1. Fluidized grain inertial flow

Fluidized grain inertial flow (coseismic) is supported by 1) the cuspate and lobate edges of MPC-wall rock contacts (Fig. 6B, 8 and 12B), 2) very fine (5–40 μm) comminuted quartz grains (Figs. 8G), 3) ultra-cataclasite preservation (Fig. 8F, 9C) and 4) plucking and sorting of wall rock clasts, 5) injection of MPC into off-fault cracks (Figs. 5–7, 12), and 6) unidirectional upward-pointing strain fringes around pyrite and hematite (Fig. 13 and C.2 E).

The intrusion and injection structures characteristic of the MPC (Figs. 1, 5, 6 and 82B, and D.1) closely resemble the morphology of fluidized layers formed during known coseismic slip (Smeraglia et al., 2017b). Fluidized layers with laminar to turbulent flow structures, cuspate-lobate margins, and injection veins have been observed elsewhere and are attributed to transient, cohesionless, low-viscosity deformation during coseismic slip (Brodsky et al., 2009; Smith et al., 2011; Fondriest et al., 2012; Tesei et al., 2013; Novellino et al., 2015; Demurtas et al., 2016; Delle Piane et al., 2017; Smeraglia et al., 2017a, 2017b, 2018; Masoch et al., 2019).

These deformation textures probably result from trapped, pressurized fluids, which can be triggered by thermal decomposition of
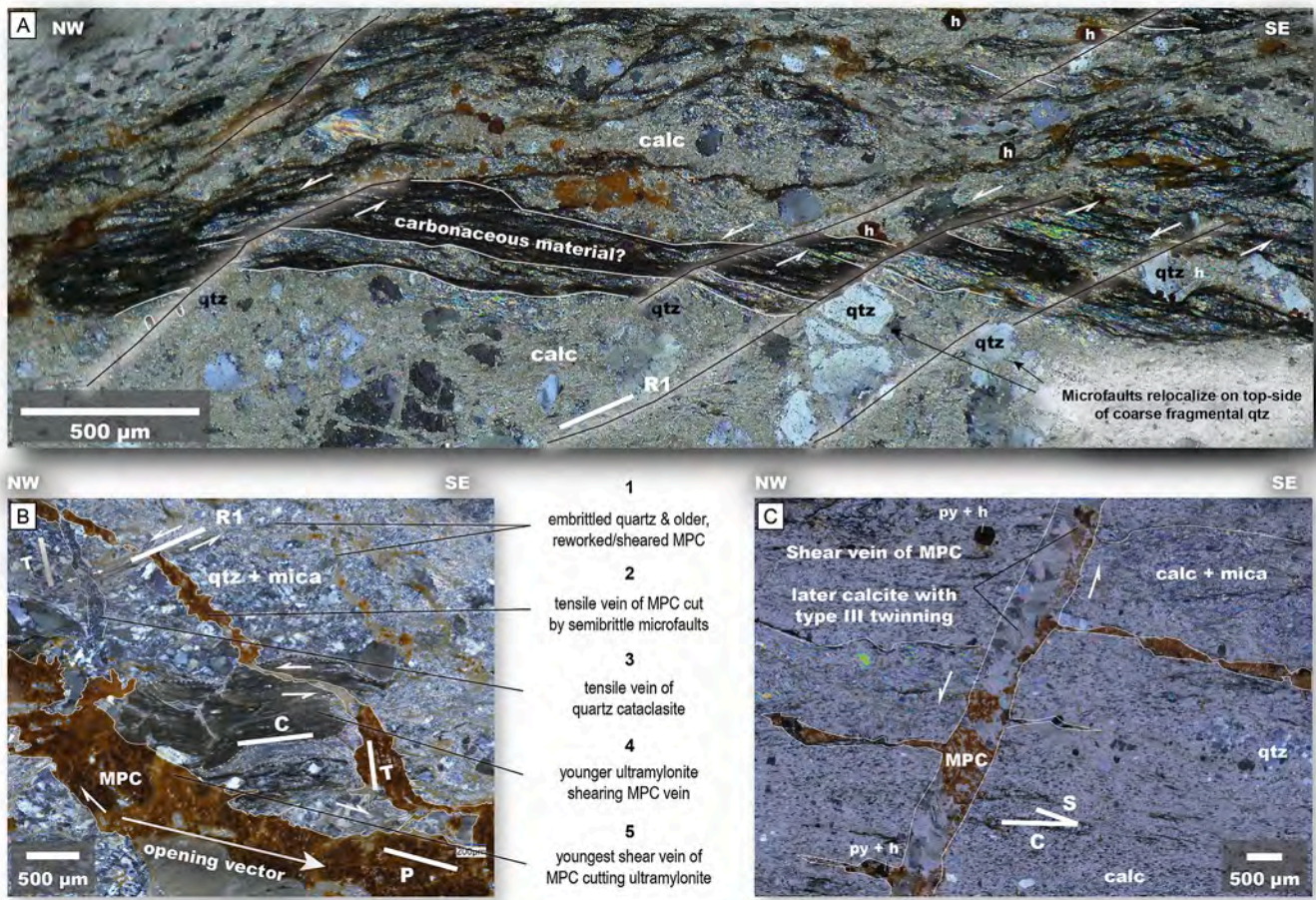
**Fig. 12.** XPL photomicrographs showing key observations of mutually overprinting brittle-ductile deformation within samples immediately beneath the BCD. For all panels, half arrows indicate shear sense and thin white lines (dashed and solid) are contacts between fault rock components. Thin black lines are R1 shears. A) Sample BCD-08an showing the relocalization of R1 microfaults on the top-NW edges of fragmental quartz grains that are randomly distributed within the flowing calc-mylonite matrix. Some putative carbonaceous material offset along the later brittle microfaults. The very fine calcite matrix is dynamically recrystallized. B) Sample BCD-08ai showing mutual overprinting between MPC veins and ultramylonite (see text for more description). The opening vector (~2 mm NW-SE) of the youngest MPC vein is based on matching the offset ultramylonite layer and a zone of coarse dynamically recrystallized quartz. C) Sample BCD-08ai showing a high angle shear vein interpreted to offset MPC and layering within calc-mylonite. The vein is filled with coarse calcite with type III twins. calc: calcite. h: hematite. py: pyrite. qtz: quartz. MPC: mixed phase cataclasite.

carbonate and clay minerals due to transient heating during coseismic slip (Han et al., 2007a, 2007b, 2010; Brantut et al., 2008; Sulem and Famin, 2009; De Paola et al., 2011; Ferri et al., 2011; Rowe et al., 2012a; Collettini et al., 2013; Platt et al., 2015b; Kim et al., 2021). Transient frictional heating is supported by the putative amorphous carbon present along R1 and Y shears within the MPC zones (Fig. 6B) and embrittled mylonite layers (Fig. 12A). If thermally mature, the speculative carbonaceous material may indicate coseismic slip (Oohashi et al., 2011, 2014; Nakamura et al., 2015; Kaneki and Hirono, 2019; Ohl et al., 2020), although such material forms during subseismic slip as well (Delle Piane et al., 2018; Kaneki et al., 2020).

Unidirectional, upward-pointing strain fringes were observed strictly within a few mm above an injected MPC vein (Fig. 13). Twite et al. (2020) interpreted these apparently rare features to indicate ascendant movement of fluid during active deformation. We suggest that the fringes represent the pressure shadow resulting from dilation during injection of the MPC. This, however, is inconsistent with studies that suggest fibres within strain fringes grow slowly over millions of years (Muller et al., 2000; Passchier and Trouw, 2005).

### 5.2.2. Thermal decomposition of pyrite

Iron oxide and/or hematite can mineralize from pyrite via low-

temperature oxidation in air or water (Zhu et al., 2018; Du et al., 2021) or via rapid thermal decomposition. While both require abundant oxygen, the latter requires temperatures and oxidation states exceeding those present within the BCD-rooted shear zone, based on the mylonitic textures. In the presence of oxic air at atmospheric pressure, a fairly high temperature range (~430–640 °C) is required to thermally decompose pyrite, oxidize the intermediate products, and form hematite (Jorgensen and Moyle, 1982; Dunn et al., 1989; Hu et al., 2006; Bhargava et al., 2009; Liu et al., 2023). High partial pressure of water vapor increases the rate of thermal decomposition and slightly decreases the temperatures at which thermal decomposition initiates (~420 °C) and completes (~630 °C) (Huang et al., 2015). These temperatures exceed those estimated at the brittle-ductile transition zone (~250–325 °C).

Therefore, we suggest that hematite within the BCD fault zone may have formed via thermal decomposition of pyrite during coseismic slip in the earthquake nucleation zone. Pyrite is systematically unaltered in calc-mylonite samples where the microstructure is well organized (Fig. C2), but completely or almost completely replaced by hematite within and adjacent to MPC veins (Fig. 8G, 9C and 13) and along brittle microfaults (Fig. 12A and 13C, and C.2). We recognize that hematite may have preferentially formed within MPC zones and along brittle microfaults simply due to supergene fluid flow that was channeled
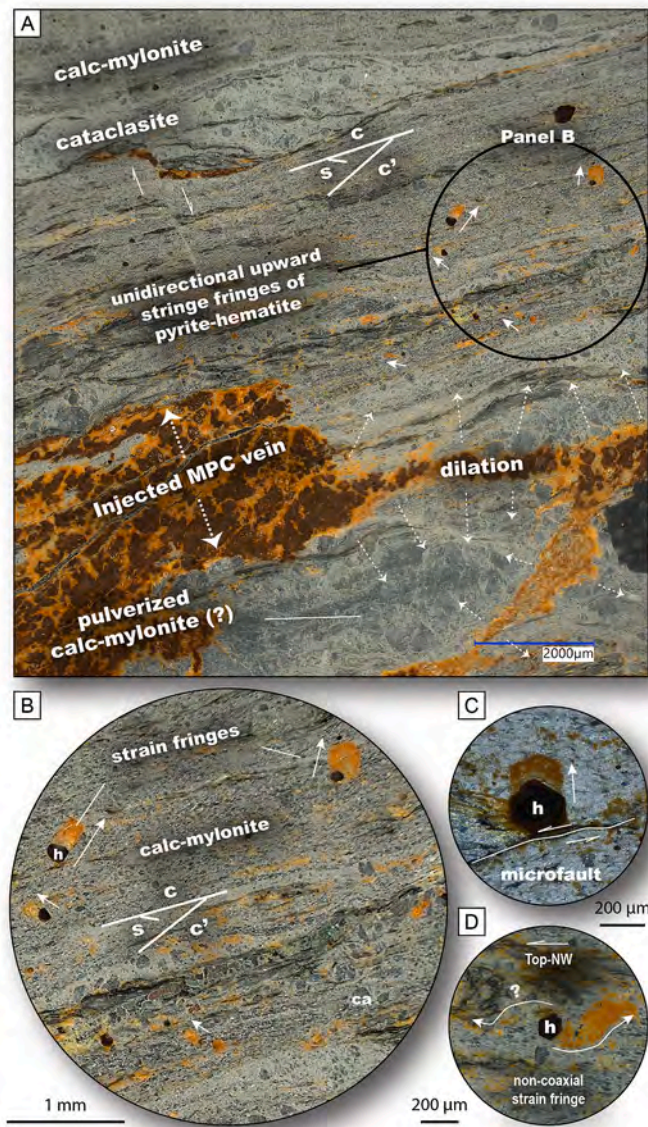
**Fig. 13.** Photomicrographs of sample BCD-08an showing unidirectional, upward pointing strain fringes above hematite adjacent to cataclastic layers within calc-mylonite. A) MPC vein injected subparallel to pre-existing C- and C′-planes. Dashed arrows illustrate the dilation around the vein. Solid arrows indicate the flow direction inferred from strain fringes. Half arrows indicate the shear sense. The high angle shear vein is the twinned calcite vein from Fig. 4F. B/C) Close-up views of unidirectional upward pointing strain fringes. D) Asymmetric, non-coaxial strain fringe around hematite suggesting rotation or sliding and indicating top-NW shear.

through these features. However, we entertain the possibility of friction-induced thermal decomposition.

### 5.2.3. Earthquake nucleation and cyclic brittle-ductile overprinting

We interpret that coseismic slip nucleated at strength contrasts within the plastically flowing calc-mylonite. This is supported by the fact that veins and shear fracture-aligned bands of MPC systematically occupy the strong-to-weak contacts across all scales, and the MPC veins have very similar composition to wall rock mylonite (Fig. 6E and 8G). The MPC zones lie between 1) quartzite breccia and mylonite at the outcrop scale (Figs. 5 and 6), 2) coarse quartz ribbons/porphyroclasts and adjacent mylonitic matrix at the mm scale (Fig. 8A, G, and 14), and 3) individual fragmental quartz survivor grains and mylonite matrix at the micron to mm scale (Fig. 8D and 12A).

Coseismic slip and formation of MPC from calc-mylonite was probably driven by some combination of 1) footwall exhumation-related cooling and 2) transient high strain rate events that caused embrittlement within the crystal-plastic fields of both calcite and quartz. The former is expected and almost certainly occurred during exhumation. However, mutually cross-cutting relationships between MPC and other fault rock components indicate that the latter occurred also. For example, Fig. 12B depicts a tensile vein of MPC that is sheared by an ~1 mm-thick ultramylonite layer, which is in turn cross-cut by a thicker shear vein of MPC with cuspate and lobate margins. The sample also contains tensile veins of quartz cataclasite.

This suggests repeated cycles of coseismic slip, MPC injection, ductile shearing, and crystal-plastic deformation. Cycles of high strain rate coseismic slip and low strain-rate crystal-plastic deformation have been proposed to explain deep fault exposures where pseudotachylyte and mylonite/ultramylonite mutually overprint one another or are interlaced (Sibson, 1980; Hobbs et al., 1986; Scholz, 1988; Koch and Masch, 1992; Lin et al., 2005; Lin, 2008; Pittarello et al., 2012; Price et al., 2012; Melosh et al., 2018), from cockade breccia (Masoch et al., 2019), and layered sequences of cataclasite (Axen et al., 2018). We suggest that the mutually overprinting MPC and ultramylonite (Fig. 12B) would invoke similar scenario.

Cyclic comminution during MPC formation and subsequent crystal plastic flow may be the mechanism by which the thin (100–500 μm) ultramylonite and ultracataclasite layers formed immediately beneath the BCD (e.g., samples BCD-08AN and BCD-08AI, Fig. 14). This process would focus stress progressively into quartz-rich domains leading to preferential cataclasis and repeated embrittlement near the interface between the weak calc-mylonite and the strong quartzite breccia layers and MPC zones. Strain localizing at this strong-weak interface, driven in part by fluid-assisted alteration and possibly high pore fluid pressure, may have led to development of the through-going BCD. High pore fluid pressure, at least during coseismic slip, is supported by injection of MPC into veins and cm-scale bands subparallel to Y, P, R1 and T (tensile) fractures (Fig. 14). Similar styles of progressive localization near the brittle-ductile transition have been interpreted from composite fault rock studies along the Whipple (Selverstone et al., 2012; Axen, 2020) and Catalina-Rincon (Davis et al., 2023) detachments. Cyclic overpressure near the brittle-ductile transition during coseismic slip, followed by a return to low levels of pore fluid pressure and dominant pressure solution/crystal-plastic flow, have been suggested also to mediate the seismic cycle (Doglioni et al., 2014; Chen et al., 2015), especially in lithologically heterogeneous fault zones (Müller et al., 2010; Tesei et al., 2013, 2014; Bullock et al., 2014).

### 5.3. Gouge: zone of aseismic creep

We infer that the foliated illite-rich gouge zones formed via aseismic creep along the BCD in the upper 5 km of crust, corresponding to $0 \leq T \leq 160\ °C$ along the reconstructed BCD. These conditions are used to build the mechanical models presented below. The gouge zones probably formed also along the upper 5 km of normal faults that sole into the BCD. The crude pinch-and-swell pattern of the foliated gouge zones relative to the (Fig. 2) suggests channeling of slip into the BCD via the gouge zones, but also occlusion of the gouge layer as slip focused into the underlying calc-mylonite layers.

## 6. Reconstructed mechanical transitions

In this section, we map out the brittle-ductile transition, earthquake nucleation zone, and zone of aseismic creep along the reconstructed BCD. We utilize existing thermo-kinematic model snapshots (Lutz et al., 2021), which constrain the fault geometry, depth of present-day fault footwall exposure, and dynamic geotherm. These constraints, when combined with the inferred thermo-genetic conditions of fault rock genesis (sections 4 and 5), allow reconstructions of the mechanical
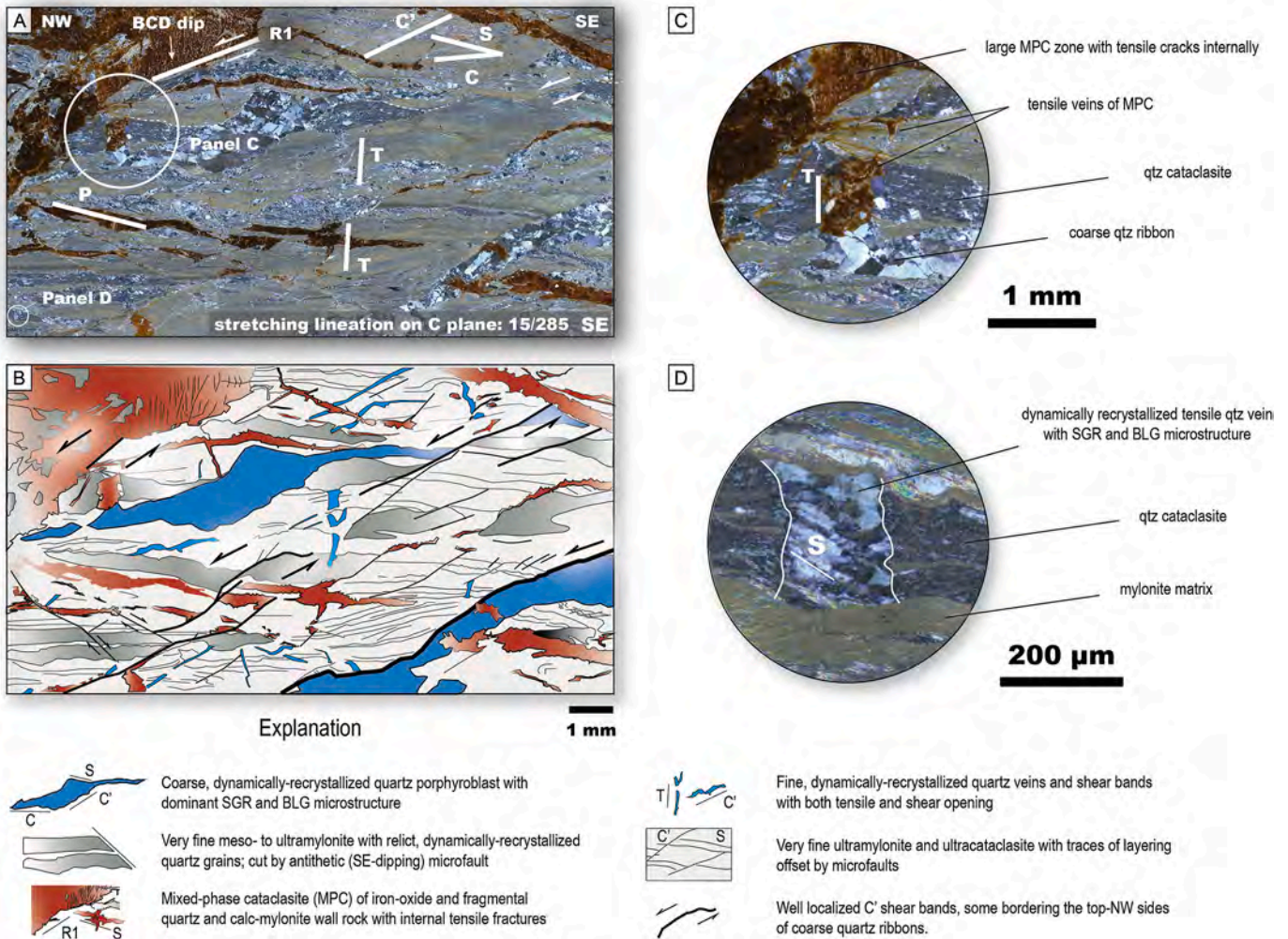
**Fig. 14.** XPL photomicrographs (A, C, D) and interpretive trace (B) showing key phases within brittle-ductile mylonite/MPC sample BCD-08ai formed immediately beneath the Boundary Canyon Detachment BCD. A) the R1 shear that parallels C′-shear bands of mylonite is subparallel to BCD dip at this location and separates thick MPC from footwall mylonite. B) Interpretation highlighting the semi-brittle microfaulting, tensile veins and shear veins filled with dynamically recrystallized quartz and MPC, and very fine ultramylonite and ultracataclasite layers. C) Relatively thick (~0.5 mm) tensile vein of MPC emanating from the coarsest part of a quartz ribbon. The vein is confined to the overlying quartz ultracataclasite and appears to smear out into the fine mylonitic matrix. D) Tensile vein confined to a quartz ultracataclasite layer that is in turn dynamically recrystallized. SGR: Subgrain rotation. BLG: Bulging recrystallization.

transitions along the fault through time.

### 6.1. Brittle-ductile transition in quartz

We interpret that the quartz brittle-ductile transition zone along the 12 Ma BCD to have been located at ~11 km depth (T = 300–325 °C) (Fig. 15A). Aside from being a standard minimum temperature of crystal plasticity in quartz (e.g., Passchier and Trouw, 2005; Fossen and Cavalcante, 2017), 325 °C corresponds to the minimum temperature of crystal-plastic flow in BCD footwall quartz mylonite based on subgrain growth modeling (Hoisch and Simpson, 1993). At depth >11 km, deformation along the initial (ca. 12 Ma) BCD was strictly plastic except for possible rapid slip events in which coseismic ruptures may have propagated into the plastic field as described in section 5.2.3 (Aharonov and Scholz, 2018, 2019).

### 6.2. Brittle-ductile transition in calcite

We interpret the calcite brittle-ductile transition zone along the 12 Ma BCD to have been located at ~9.5 km depth (T = 250 °C) (Fig. 15A). The 250 °C isotherm is the inferred minimum temperature of crystal-plastic flow of calcite, based in part on the average grain size of

bulges in calc-mylonite (7.65 ± 1.5 μm; Fig. 4D), the temperature calibration study of Ebert et al. (2008), and the assumption that some post-mylonitic grain growth may have taken place such that our mean grain size (average 12.45 ± 1.5 μm) is slightly too high (e.g., Beyene (2011) measured calcite grains as small as 3–5 μm).

Thus, at temperatures between 250 and 325 °C, corresponding to 9.5–11 km depth along the initial BCD, plastic flow of calc-mylonite and brittle fracturing of quartz were contemporaneous. This is supported by several observations at outcrop (Figs. 3C and 5E) to microscopic (Fig. 4A, F, 12, and 14) scales. Therefore, cataclasis and brittle slip within the 9.5–11 km depth range were possible, especially along patches with abundant quartz-bearing protoliths. Furthermore, experiments suggest that brittle stick slip and cataclasite flow of calcite may occur within the nominally plastic field (at T ≤ 500 °C) due to sufficiently fast slip rates (≥0.3 μm/s), and the resultant fault rock may be indistinguishable from a calc-mylonite (Verberne et al., 2015; Chen et al., 2020; Del Sole et al., 2023).

### 6.3. Earthquake nucleation zone

The main earthquake nucleation zone was probably located between 5 and 9.5 km depth along the initial BCD, corresponding to 160 °C ≤ T ≤
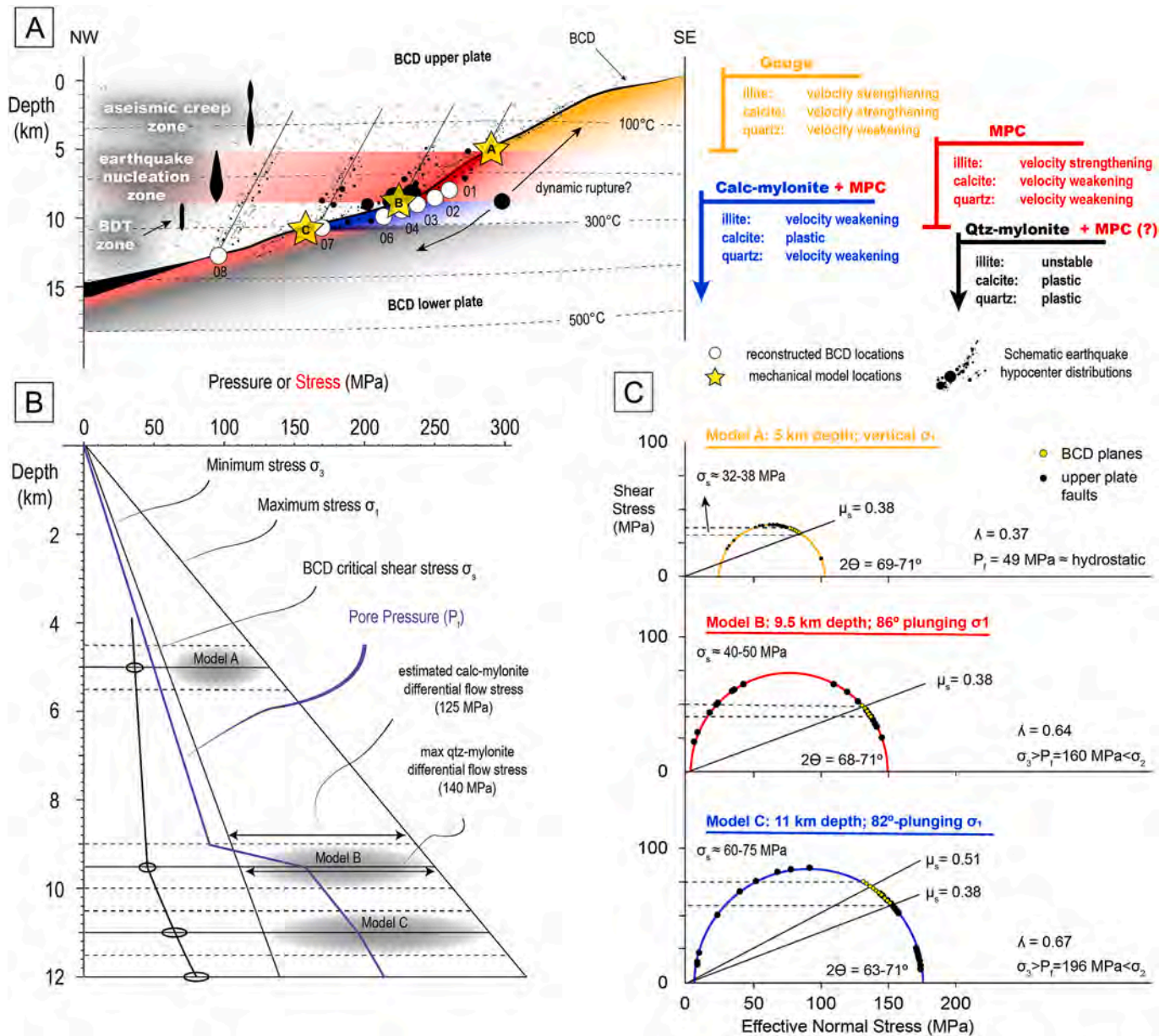
**Fig. 15.** Mechanical models of BCD fault slip. A) Fault rock zones mapped onto the 12 Ma snapshot of thermo-kinematic reconstructions (Lutz et al., 2021). Yellow stars show the depths where static stress models were analyzed. B) Modeled pressure profile showing the linear principal stress gradients ($\sigma_1$ and $\sigma_3$), pore fluid pressure ($P_f$), and BCD critical shear stress calculations ($\sigma_s$). C) Mohr diagrams showing preferred stress state and failure envelopes for the BCD and hanging wall faults at various depths. Fault planes binned within 500 m of the depth location of each model. BDT: Brittle-ductile transition. EQ: earthquake. MPC: Mixed phase cataclasite. qtz: quartz. $\mu_s$: coefficient of static friction. $\lambda$: ratio of pore fluid pressure to the maximum principal stress ($\sigma_1$). $\Theta$: angle between the maximum stress ($\sigma_1$) and the fault. (For interpretation of the references to color in this figure legend, the reader is referred to the Web version of this article.)

250 °C (Fig. 15A). We infer that this was the main zone in which MPC formed via coseismic slip along the BCD based on the rate-state behavior of the primary mineral phases within MPC: calcite, quartz, and illite.

Calcite. Calcite, the dominant phase in the immediate BCD footwall from our observations (Fig. 2), is velocity weakening and would nucleate stick slip instabilities within the 160 °C < T < 250 °C zone. This supports earthquake nucleation within this temperature range. Velocity weakening, stick slip, and granular flow were observed in experiments on calcite gouge at 100 °C < T < 550 °C for slip velocities <3 μm/s (Verberne et al., 2015; Chen et al., 2020). These experiments suggest that the fine grained calc-mylonite along the BCD could have been formed by a combination of frictional sliding (stick slip) and plastic flow. Other experiments performed at higher slip rates (~1 m/s) yielded velocity weakening behavior only after sufficient development of a

fine-grained high shear band (Smith et al., 2015). Lacey (2018) showed with frictional hold-slide experiments that calcite in marble exhibits velocity-strengthening behavior and stable dissolution-creep at 30 °C < T < 70 °C, oscillatory, slow-slip behavior at 70 °C < T < 160 °C, and velocity-weakening, stick-slip behavior at 160 °C < T < 300 °C.

**Quartz.** Laboratory experiments and representative analytical models suggest that quartz and quartz-illite gouge exhibit velocity weakening behavior at T > 150 °C if slip rates are fast enough (e.g., mm/s) and slip distance is great enough (cm) (Di Toro et al., 2004; Nakatani and Scholz, 2004; Niemeijer and Spiers, 2007).

Illite. Abundant mechanical experiments performed on illite and illite-rich gouge have demonstrated velocity strengthening behavior at T < 250 °C across a wide range of stress conditions and sliding velocities (Moore et al., 1989; Saffer and Marone, 2003; den Hartog et al., 2012a,

2012b, 2013; den Hartog and Spiers, 2013; Tesei et al., 2015; Okuda et al., 2023).

### 6.4. Zone of aseismic creep

The zone of aseismic creep and stable sliding where earthquake presumably could not nucleate was probably located between 0 and 5 km depth along the initial BCD, corresponding to T < 160 °C (Fig. 15A). At T < 160 °C, illite and calcite exhibit velocity strengthening behavior (see above). We interpret that the thick zones of foliated, illite-rich fault gouge were formed in this zone throughout BCD slip and footwall exhumation.

## 7. Static stress models at mechanical transitions

### 7.1. Depth-dependent static friction

Static friction ($\mu_s$) was assigned to different parts of the initial BCD through comparison of fault rock compositions to thermally controlled laboratory experiments. Illite is the weakest phase in the BCD fault rocks. Illite comprises 25–50% of most foliated gouge and up to 90% along Y, R1, and P shears (Fig. 11 and B2). Illite-rich gouge (65% illite) has $\mu_s$ = 0.28–0.51 (Behnsen and Faulkner, 2012; den Hartog et al., 2012b, 2013; den Hartog and Spiers, 2013; Haines et al., 2013, 2014; Mariani et al., 2015). Experiments that were run at high normal stress (>100 MPa) and with pore fluid pressure (Behnsen and Faulkner, 2012; den Hartog et al., 2013) yielded $\mu_s$ = 0.38. Illite comprises 20–50% of the MPC that was analyzed by XRD (Fig. 6E) and electron microprobe analyses (Fig. 8G), suggesting $\mu_s$ = 0.38–0.51 (Tembe et al., 2010; den Hartog et al., 2013). Therefore, failure envelopes in static stress models utilize a range of static friction coefficients (0.38≤$\mu_s$ ≤ 0.51). The moderate friction range ($\mu_s$ = 0.38–0.51) was used in relatively deep models (11–12 km). We used the relatively low friction ($\mu_s$ = 0.38) in shallow models (0–9.5 km).

### 7.2. Depth-dependent static stress

Modeling results show that shear stress along the BCD increases linearly in the upper crust, but this linearity breaks down near the brittle-ductile transition due to plunging $\sigma_1$, elevated friction, and pore fluid pressure (Fig. 15B and C). Moderate rotation of the stress field to plunge 60–80° NW toward the hanging wall transport direction is consistent with reconstruction of mylonitic fabrics in the BCD root (Hoisch and Simpson, 1993; Lutz et al., 2021), including possible conjugate fractures within calc-mylonite that may have formed contemporaneously with mylonitic flow (Fig. 4B and D.2). Elevated pore fluid pressure near the upper brittle-ductile transition is possible, considering the abundance of tensile and shear veins filled with dynamically recrystallized and/or type III twinned calcite (Fig. 4A, F, and 12C), dynamically recrystallized quartz (Fig. 14D), and MPC (Figs. 5, 6, 12 and 14) and the general lack of such veins in up-dip BCD locations (Fig. 3D and E).

Many combinations of stress field orientation ($\sigma_1$ plunge from 60 to 80° NW), coefficient of static friction (0.38 ≤ $\mu_s$ ≤ 0.51), and pore fluid pressure (0.37 ≤ $\lambda$ ≤ 0.68) may have induced shear failure along the reconstructed BCD. The configurations shown in Fig. 15 are probable scenarios that are supported by the fault rock observations (section 4) and interpretations (section 5).

Model A. This model was generated at depth = 5 km (T ≈ 160 °C) and is inferred to represent the maximum shear stress of stable sliding within the aseismic creep zone where foliated gouge was forming (Fig. 15). Low shear stress ($\sigma_s$ ≈ 32–38 MPa) was calculated using vertical maximum stress ($\sigma_1$ ≈ 132 MPa), hydrostatic pore fluid pressure ($\lambda$ = 0.37; $P_f$ ≈ 49 MPa), low fault dip (22° ≤ $\delta$ ≤ 30°), and moderately low static friction ($\mu_s$ = 0.38).

Model B. This model was generated at depth = 9.5 km (T ≈ 250 °C)

and is inferred to represent the maximum shear stress along that fault near the top of the brittle-ductile transition for calcite in calc-mylonite below the BCD. Elevated shear stress ($\sigma_s$ ≈ 40–50 MPa) was calculated using an 86°-plunging maximum stress ($\sigma_1$ ≈ 250 MPa), elevated pore fluid pressure ($\lambda$ = 0.64; $P_f$ ≈ 160 MPa), low fault dip (15° ≤ $\delta$ ≤ 20°), and the range of static friction estimated for the MPC zones (0.38≤$\mu_s$ ≤ 0.51). The differential stress at this model depth is ~140 MPa, which is consistent with the maximum stress of crystal-plastic flow in quartz mylonite, but may be slightly less than the maximum stress of crystal-plastic flow in calc-mylonite, depending on the assumptions about grain size piezometry and annealing after grain size reduction (section 4.1).

This model supports that, within the plastic flow field for calcite (>9.5 km depth), stress preferentially transferred to or was supported within quartz-rich domains (e.g., porphyroclasts and ribbons). Focusing of stress into quartz-rich domains is substantiated by brittle-ductile textures from the outcrop to microscopic scale (Fig. 3C, 4A and 5E, 6B, and 14). Similar stress configurations have been shown or interpreted in recent laboratory experiments on mixed clay-quartz gouge (Bedford et al., 2022) and from field studies of extensional detachments formed in mixed clastic-carbonate protoliths (Singleton et al., 2018). We infer that this mechanical heterogeneity promoted nucleation of stick-slip instabilities near quartz-rich domains within the brittle-ductile transition zone.

Model C. This model was generated at depth = 11 km (T ≈ 300–325 °C) and is inferred to represent the shear stress along the fault near the top of the brittle-ductile transition for quartz in calc-mylonite below the BCD. High shear stress ($\sigma_s$ ≈ 60–75 MPa) was calculated using an 82°-plunging maximum stress ($\sigma_1$ ≈ 295 MPa), elevated pore fluid pressure ($\lambda$ = 0.67; $P_f$ ≈ 196 MPa), low fault dip (15° ≤ $\delta$ ≤ 20°), and the range of static friction estimated for the MPC zones (0.38 ≤ $\mu_s$ ≤ 0.51). We recognize that friction may have been higher if quartz was the primary control, and therefore the shear stress calculated in Model C may be an underestimate.

## 8. Discussion

### 8.1. Seismogenic low-angle slip

We have presented several convincing lines of evidence to support normal-sense, coseismic slip along the reconstructed low-angle BCD (see section 5.2). Coseismic slip along low-angle normal faults is favored by some combination of the following mechanisms: 1) pore fluid overpressure due to fault healing and permeability reduction (fault valve model) (Sibson, 1992, 2019), 2) rotation of the maximum stress in the deep brittle crust to reduce the angle between the maximum stress and the fault (Spencer and Chase, 1989; Yin, 1989; Axen, 1992, 2020; Wernicke, 1992; Westaway, 1999), and/or 3) stress increase from locked, interconnected, and super-critically stressed fault networks (Fletcher et al., 2016).

Our 2D static stress models permit any combination of these potential factors. Despite moderate friction (0.38 ≤ $\mu_s$ ≤ 0.51), some minor rotation of the stress field (10–20°) and/or elevated pore fluid pressure ($P_f$ = 100–200 MPa; 0.37 ≤ $\lambda$ ≤ 0.68) were probably needed to induce shear failure on the modeled low-angle (<19°) BCD at depth >6 km (Fig. 15C). Pore fluid pressure was almost certainly very high during injection of the MPC veins, which occupy T, Y, S, and R1 planar orientations (Figs. 8 and 12–14). Furthermore, high-angle hanging wall normal faults that sole into the BCD (Fig. 10A and 15A) were super-critically stressed at conditions where the BCD was sub-critically to critically stressed (Fig. 15C).

Thus, it seems likely that the BCD was a "keystone" fault (Fletcher et al., 2016) during seismic faulting events, initiating dynamic rupture of super-critically stressed, but geometrically locked, fault networks. We envision a scenario where deep plastic flow and shallow aseismic creep promoted stress concentration along the stronger, frictionally locked,

and/or poorly oriented patches of the BCD. Quartz-rich domains within and bounding flowing calc-mylonite eventually failed frictionally, leading to nucleation of a stick-slip instability and dynamic rupture propagation up dip through the velocity-strengthening patches (Faulkner et al., 2011; Collettini et al., 2019) and down dip through the plastically flowing BCD root (Hobbs et al., 1986; Scholz, 1988; Aharonov and Scholz, 2018, 2019). Coseismic rupture in the otherwise crystal-plastic field (T ≥ 325 °C, depth ≥9.5 km) is supported by mutually cross-cutting relationships preserved between MPC veins, semi-brittle microfaults, and ultramylonite layers immediately beneath the BCD (Fig. 2A and 14). Dynamic rupture propagation up dip through the velocity-strengthening patches may explain the formation of the pulverized gouge at BCD-02 and BCD-03 (Fig. 2E, F, and 10B).

### 8.2. Thin earthquake nucleation zone

The inferred earthquake nucleation zone along the BCD both thinned and shallowed with exhumation. Heat advected with the rising footwall increased the average upper crustal geotherm from ~27 °C/km at initiation (ca. 12 Ma; Fig. 16A) to ~40 °C/km locally by exhumation (ca. 7 Ma; Fig. 16C). This elevated the tops of the calcite brittle-ductile transition and earthquake nucleation zone to ~5 km depth and ~3.5–5 km depth, respectively. The very shallow upper brittle-ductile transition and thin earthquake nucleation zone would severely limit the fault's capacity to host large magnitude earthquakes. This thin earthquake nucleation zone may have been completely absent as the geotherm was compressed, especially if the calc-mylonite along the BCD underwent crystal-plastic deformation at very low temperatures (≥150 °C) (Kennedy and White, 2001).

Thin earthquake nucleation zones may be common to continental low-angle normal faults, especially those developed in thick sections of relatively fine-grained and mixed carbonate-siliciclastic rocks. In such upper crustal sections, the zones of low-temperature plasticity in carbonates and aseismic creep along reaction-weakened clastics (clay-rich gouge) may amalgamate (Lutz et al., 2021). This would lower potential earthquake magnitude by reducing nucleation width and limiting dynamic rupture potential (Kaneko and Lapusta, 2010; Avouac, 2015; Scholz, 2019). Pervasive hanging wall damage from faulting and fracturing contributes also to small earthquake nucleation zones through enhanced fault-parallel hydraulic conductivity. Overwhelming evidence of deep meteoric water circulation into detachment shear zones (Fricke et al., 1992; Morrison, 1994; Gébelin et al., 2015; Haines et al., 2016; Bons and Gomez-Rivas, 2020; Dusséaux et al., 2022) supports that reaction softening via authigenesis and phyllosilicate development is a viable, widespread mechanism to weaken faults and allow slip under non-Andersonian conditions (Massironi et al., 2011; Collettini et al., 2019). However, due to slip stabilization and restrengthening under hydrothermal conditions, the earthquake nucleation zone may deepen and strengthen with time (Chen et al., 2015).

### 8.3. Future work

The BCD preserves fault rocks that formed during processes spanning much of the upper crust. Beyond what is presented here, these naturally deformed rocks can inform the mechanics of cyclic coseismic-aseismic deformation 1) near the strong brittle-ductile transition where large earthquakes tend to nucleate, and 2) within clay-dominated creeping fault sections through which dynamic ruptures may propagate.

Further work on the BCD fault rocks will help constrain these processes and expand our understanding of cyclic coseismic-aseismic deformation along low-angle normal faults. This work may involve electron backscatter diffraction (EBSD) and 3D measurements of calcite twinning to develop more robust constraints on the temperature and stress state near the brittle-ductile transitions for both quartz and calcite in the system. EBSD analyses could confirm our preliminary grain size measurements made on a petrographic microscope and could reveal
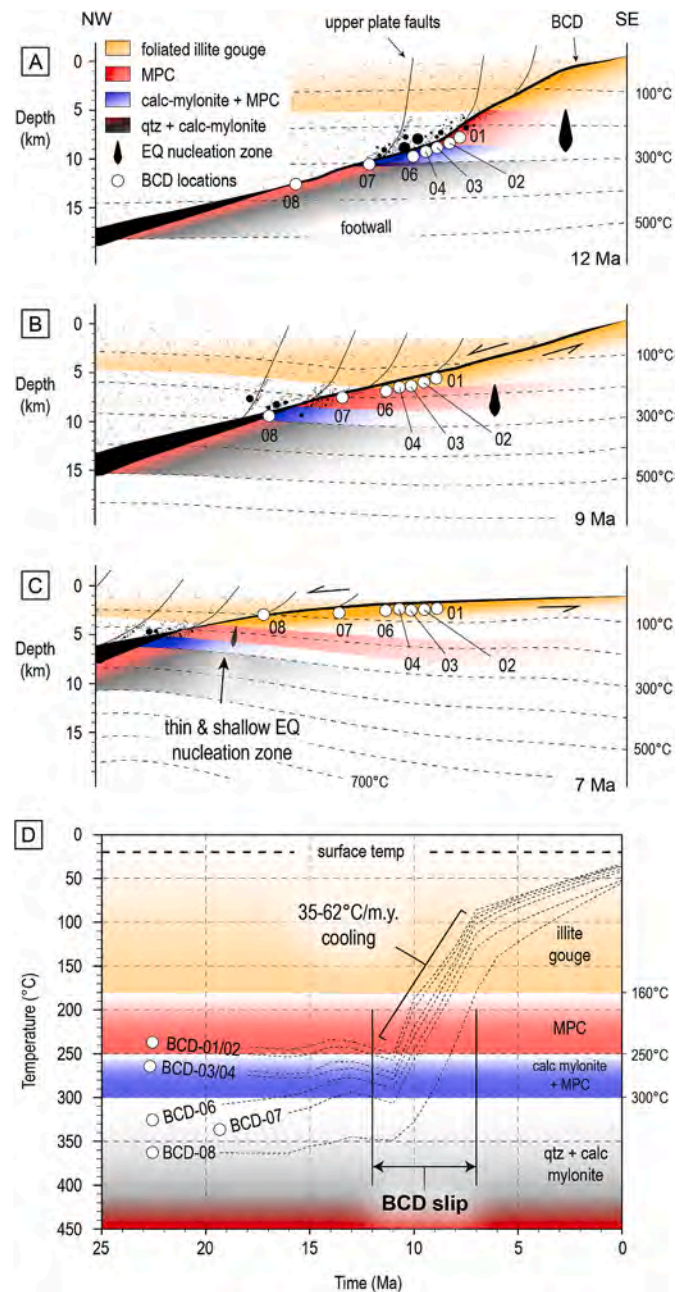


**Fig. 16.** Reconstructed temperature-time-depth evolution of BCD study locations from initiation (A) to exhumation (C). A) Initial BCD (ca. 12 Ma; same as Fig. 15A). B) 9 Ma thermo-kinematic model snapshot showing initial footwall exhumation and passage of structurally highest BCD footwall locations (BCD-01-04) into the creeping zone. Locations BCD-07 and -06 enter the earthquake nucleation zone, and BCD-08 exits the plastic field for quartz. C) 7 Ma thermo-kinematic model snapshot showing further footwall exhumation and passage of structurally deeper BCD footwall locations (BCD-06-08) through the very thin earthquake nucleation zone and into the creeping zone. Symbols and colors the same as Fig. 15. D) Thermal evolution of BCD study locations based on thermo-kinematic models of Lutz et al. (2021). EQ: earthquake. MPC: mixed phase cataclasite. qtz: quartz. (For interpretation of the references to color in this figure legend, the reader is referred to the Web version of this article.)

combined crystallographic- and shape-preferred orientations of calcite, a texture that may indicate coseismic slip (Smith et al., 2013; Novellino et al., 2015). However, similar fabrics have been observed in experiments conducted at sub-seismic slip rates (Verberne et al., 2015) and rocks deformed by natural aseismic creep.

Combined SEM and transmission electron microscopy (TEM)

imaging of the MPC, especially along sharp cuspate-lobate wall-rock contacts (e.g., Figs. 1, 6 and 82B), will inform the micro-to nano-scale grain fabrics of calcite, phyllosilicates, hematite, and any other oxides or hydroxides within the MPC. We predict that such imaging of the fluidized layers will reveal features such as skeletal calcite (Collettini et al., 2013; Delle Piane et al., 2017), nanospherules and nanotubes of phyllosilicate (e.g., Smeraglia et al., 2017b, 2017a), and amorphous silica (Collettini et al., 2013). Presence of these nano-scale components would bolster our interpretations of coseismic low-angle slip. Raman spectroscopy of the black material focused along Y and R1 shears within MPC (Fig. 6B) and C-planes within calc-mylonite (Fig. 12A) would confirm the presence of amorphous carbon and reveal if it has matured thermally due to frictional heating.

Calcite within the fault zone is pre- syn- and post-kinematic. This presents an excellent opportunity to utilize in-situ calcite U–Pb dating (Roberts and Walker, 2016; Hansman et al., 2018; Bilau et al., 2020; Amidon et al., 2022; Roberts and Holdsworth, 2022) to constrain the age of deformation and compare with existing thermo-kinematic modeling. In particular, the twinned and dynamically recrystallized calcite would provide estimates of ductile deformation, and late-stage vein calcite within MPC and breccia layers would constrain the minimum age of cataclastic deformation within the earthquake nucleation zone.

The general lack of a continuous, localized principal slip surface along the BCD is puzzling and conjures several important questions related to 1) our treatment of the fault in mechanical models and 2) formation of a throughgoing detachment surface. One outstanding question is: did the BCD slip surface relocate repeatedly within the fault's general shear zone (mylonite and gouge zones) such that there was no long-lived detachment?

Without a well-localized slip surface along the detachment, the large (~35 km) net heave was probably accommodated by distributed, interseismic shear within meter's-thick layers of 1) clay-rich gouge at the base of the hanging wall and 2) quartz and calc-mylonite at the top of the footwall. Conversely, punctuated seismic slip that propagated through these generally weak shear zones may have produced 1) dolostone breccia and pulverized gouge at the base of the hanging wall and 2) MPC and quartzite breccia at the top of the footwall. Punctuated coseismic slip events, focused within the earthquake nucleation zone (Fig. 15A), may have acted to link the weak fault patches dominated by creep- and plastic flow, forming a high-friction ramp. This linkage may have formed temporary through-going detachments that are subsequently abandoned and incorporated into the weak general shear zones.

Detailed geologic mapping of the hanging wall/footwall lithologies and the fault rock types would help confirm or reject several the hypotheses we present for the sources of the clay-rich gouge zones and help understand the sub-km scale of the BCD and its incision/excision history.

## 9. Conclusions

We integrate field, microstructural, and geochemical observations of fault rocks with existing thermo-kinematic models to understand the mechanical evolution of an exhumed low-angle normal fault, the Boundary Canyon detachment (BCD). The BCD offers an unprecedented view into brittle, ductile, and mixed mode deformation along a low-angle normal fault hosted in varied host rocks (metapelite, carbonate, clastic). The following conclusions are reached.

(1) The BCD produced a heterogeneous suite of fault rocks, including quartz- and calc-mylonite, cataclasite, foliated illite-rich gouge, pulverized gouge, and various types of breccia.
(2) Injection veins, fluidized granular flow textures, unidirectional, upward pointing strain fringes, and pulverized gouge support coseismic slip along the BCD, which appears to have nucleated at inherited strength contrasts both within and surrounding weak calc-mylonite layers (i.e., quartz ribbons, quartzite breccia layers, porphyroclasts).
(3) Static stress models support that the initial (ca. 12 Ma) fault crept at $<$30–38 MPa shear stress in the uppermost crust (depth $<$5 km) but may have slipped coseismically at 40–75 MPa along deeper fault patches (~5–11 km depth).
(4) Despite relatively low friction ($0.38 \leq \mu_s \leq 0.51$), rotation of the stress field (~10–20° from vertical) and elevated pore fluid pressure ($P_f$ = 100–200 MPa; $0.37 \leq \lambda \leq 0.68$) were probably needed to induce shear failure along the low-angle ($<$19° dip) BCD fault patches.
(5) High-angle hanging wall faults were super-critically stressed when the BCD was (sub) critically stressed, suggesting that the BCD was a "keystone" fault (Fletcher et al., 2016) and triggered dynamic ruptures.
(6) The BCD cut through a thin earthquake nucleation zone (0-4 km-thick vertically) that shallowed and thinned as heat was advected with the exhuming footwall.

## CRediT authorship contribution statement

## Declaration of competing interest

The authors declare that they have no known competing financial interests or personal relationships that could have appeared to influence the work reported in this paper.

## Data availability

Data will be made available on request.

## Acknowledgements

## Appendix A. Supplementary data

Supplementary data to this article can be found online at https://doi.org/10.1016/j.jsg.2024.105132.

# References

Abers, G.A., 2001. Evidence for Seismogenic Normal Faults at Shallow Dips in Continental Rifts, vol. 187. Geological Society, London, Special Publications, pp. 305–318.

Affinati, S.C., Hoisch, T.D., Wells, M.L., Vervoort, J.D., 2020. Pressure-temperature-time paths from the Funeral Mountains, California, reveal Jurassic retroarc underthrusting during early Sevier orogenesis. Geol. Soc. Am. Bull. 132 https://doi.org/10.1130/B35095.1.

Affinati, S.C., Hoisch, T.D., Wells, M.L., Wright, S., 2022. Retroarc Jurassic burial and exhumation of Barrovian metamorphic rocks dated by monazite petrochronology, Funeral Mountains, California. In: Craddock, J.P., Malone, D.H., Foreman, B.Z., Konstantinou, A. (Eds.), Tectonic Evolution of the Sevier-Laramide Hinterland, Thrust Belt, and Foreland, and Postorogenic Slab Rollback (180–20 Ma), vol. 555. Geological Society of America Special Paper, Boulder, Colorado, p. 20. https://doi.org/10.1130/2021.2555(01.

Aharonov, E., Scholz, C.H., 2018. A physics-based rock friction constitutive law: steady state friction. J. Geophys. Res. Solid Earth 123, 1591–1614.

Aharonov, E., Scholz, C.H., 2019. The brittle-ductile transition predicted by a physics-based friction law. J. Geophys. Res. Solid Earth 124, 2721–2737.

Amidon, W.H., Kylander-Clark, A.R.C., Barr, M.N., Graf, S.F.I., West Jr, D.P., 2022. Pace of passive margin tectonism revealed by U-Pb dating of fracture-filling calcite. Nat. Commun. 13, 1953.

Amontons, G., 1699, Mémoires de l'Académie Royale: , p. 257–282..

Anderlini, L., Serpelloni, E., Belardinelli, M.E., 2016. Creep and locking of a low-angle normal fault: insights from the Altotiberina fault in the northern Apennines (Italy). Geophys. Res. Lett. 43, 4321–4329.

Applegate, J.D.R., Hodges, K.V., 1995. Mesozoic and Cenozoic extension recorded by metamorphic rocks in the Funeral Mountains, California. Geol. Soc. Am. Bull. 107 https://doi.org/10.1130/0016-7606(1995)107<1063:MACERB>2.3.CO;2.

Avouac, J.-P., 2015. From geodetic imaging of seismic and aseismic fault slip to dynamic modeling of the seismic cycle. Annu. Rev. Earth Planet Sci. 43, 233–271.

Axen, G.J., 1992. Pore pressure, stress increase, and fault weakening in low-angle normal faulting. J. Geophys. Res. Solid Earth 97, 8979–8991.

Axen, G.J., 1999. Low-angle normal fault earthquakes and triggering. Geophys. Res. Lett. 26, 3693–3696.

Axen, G.J., 2004. Mechanics of low-angle normal faults. In: Karner, G.D., Morris, J.D., Driscoll, N.W., Silver, E.A. (Eds.), Rheology and Deformation of the Lithosphere at Continental Margins, MARGINS Theoretical and Experimental Earth Science Series, pp. 46–91.

Axen, G.J., 2007. Research focus: significance of large-displacement, low-angle normal faults. Geology 35, 287–288.

Axen, G.J., 2020. How a strong low-angle normal fault formed: the Whipple detachment. Southeastern California: GSA Bulletin 132, 1817–1828.

Axen, G.J., Selverstone, J., 1994. Stress State and Fluid-Pressure Level along the Whipple Detachment Fault, vol. 22. California, Geology, pp. 835–838.

Axen, G.J., Selverstone, J., Luther, A., 2018. A rock record of paleoseismic cycling: unique layered cataclasites below the West Salton detachment fault, southern California. Geosphere 14, 187–214.

Barnes, P.M., Wallace, L.M., Saffer, D.M., Bell, R.E., Underwood, M.B., Fagereng, A., Meneghini, F., Savage, H.M., Rabinowitz, H.S., Morgan, J.K., 2020. Slow slip source characterized by lithological and geometric heterogeneity. Sci. Adv. 6, eaay3314.

Bedford, J.D., Faulkner, D.R., Lapusta, N., 2022. Fault rock heterogeneity can produce fault weakness and reduce fault stability. Nat. Commun. 13, 326.

Behnsen, J., Faulkner, D.R., 2012. The effect of mineralogy and effective normal stress on frictional strength of sheet silicates. J. Struct. Geol. 42, 49–61.

Berthé, D., Choukroune, P., Jégouzo, P., 1979. Orthogneiss, mylonite and non coaxial deformation of granites: the example of the South Armorican Shear Zone. J. Struct. Geol. 1, 31–42.

Beyene, M.A., 2011. Mesozoic Burial, Mesozoic and Cenozoic Exhumation of the Funeral Mountains Core Complex, Death Valley, Southeastern California [Ph.D. Thesis]. University of Nevada, Las Vegas, p. 362.

Bhargava, S.K., Garg, A., Subasinghe, N.D., 2009. In situ high-temperature phase transformation studies on pyrite. Fuel 88, 988–993.

Biemiller, J., Gabriel, A., Ulrich, T., 2022. The dynamics of unlikely slip: 3D modeling of low-angle normal fault rupture at the mai'iu fault, Papua New Guinea. G-cubed 23, e2021GC010298.

Bilau, A., Rolland, Y., Schwartz, S., Godeau, N., Guihou, A., Deschamps, P., Brigaud, B., Noret, A., Dumont, T., Gautheron, C., 2020. Extensional reactivation of the Penninic Frontal Thrust 3 Ma ago as evidenced by U-Pb dating on calcite in fault zone cataclasite. Solid Earth Discussions 2020, 1–24.

Boncio, P., Brozzetti, F., Lavecchia, G., 2000. Architecture and seismotectonics of a regional low-angle normal fault zone in central Italy. Tectonics 19, 1038–1055.

Bons, P.D., Gomez-Rivas, E., 2020. Origin of meteoric fluids in extensional detachments. Geofluids 2020, 1–8.

Borradaile, G.J., 1981. Particulate flow of rock and the formation of cleavage. Tectonophysics 72, 305–321.

Brantut, N., Schubnel, A., Rouzaud, J., Brunet, F., Shimamoto, T., 2008. High-velocity frictional properties of a clay-bearing fault gouge and implications for earthquake mechanics. J. Geophys. Res. Solid Earth 113.

Brodsky, E.E., Rowe, C.D., Meneghini, F., Moore, J.C., 2009. A geological fingerprint of low-viscosity fault fluids mobilized during an earthquake. J. Geophys. Res. Solid Earth 114.

Brodsky, E.E., Gilchrist, J.J., Sagy, A., Collettini, C., 2011. Faults smooth gradually as a function of slip. Earth Planet Sci. Lett. 302, 185–193.

Brozzetti, F., Boncio, P., Lavecchia, G., Pace, B., 2009. Present activity and seismogenic potential of a low-angle normal fault system (Città di Castello, Italy): Constraints from surface geology, seismic reflection data and seismicity. Tectonophysics 463, 31–46.

Bullock, R.J., De Paola, N., Holdsworth, R.E., Trabucho-Alexandre, J., 2014. Lithological controls on the deformation mechanisms operating within carbonate-hosted faults during the seismic cycle. J. Struct. Geol. 58, 22–42.

Burkhard, M., 1993. Calcite twins, their geometry, appearance and significance as stress-strain markers and indicators of tectonic regime: a review. J. Struct. Geol. 15, 351–368.

Caine, J.S., Forster, C.B., 1999. Fault zone architecture and fluid flow: insights from field data and numerical modeling. Geophys. Monograph-Am. Geophys. Union 113, 101–128.

Caine, J.S., Minor, S.A., 2009. Structural and geochemical characteristics of faulted sediments and inferences on the role of water in deformation, Rio Grande Rift, New Mexico. Geol. Soc. Am. Bull. 121, 1325–1340.

Caine, J.S., Bruhn, R.L., Forster, C.B., 2010. Internal structure, fault rocks, and inferences regarding deformation, fluid flow, and mineralization in the seismogenic Stillwater normal fault, Dixie Valley, Nevada. J. Struct. Geol. 32, 1576–1589.

Caine, J.S., Minor, S.A., Grauch, V.J.S., Budahn, J.R., Keren, T.T., 2017. A comprehensive survey of faults, breccias, and fractures in and flanking the eastern Española Basin, Rio Grande rift, New Mexico. Geosphere 13, 1566–1609.

Chen, J., Verberne, B.A., Spiers, C.J., 2015. Interseismic re-strengthening and stabilization of carbonate faults by "non-Dieterich" healing under hydrothermal conditions. Earth Planet Sci. Lett. 423, 1–12.

Chen, J., Verberne, B.A., Niemeijer, A.R., 2020. Flow-to-friction transition in simulated calcite gouge: experiments and microphysical modeling. J. Geophys. Res. Solid Earth 125, e2020JB019970.

Chiaraluce, L., Chiarabba, C., Collettini, C., Piccinini, D., Cocco, M., 2007. Architecture and mechanics of an active low-angle normal fault: alto Tiberina fault, northern Apennines, Italy. J. Geophys. Res. Solid Earth 112.

Collettini, C., 2011. The mechanical paradox of low-angle normal faults: current understanding and open questions. Tectonophysics 510, 253–268.

Collettini, C., Holdsworth, R.E., 2004. Fault zone weakening and character of slip along low-angle normal faults: insights from the Zuccale fault, Elba, Italy. J. Geol. Soc. 161, 1039–1051.

Collettini, C., Viti, C., Tesei, T., Mollo, S., 2013. Thermal decomposition along natural carbonate faults during earthquakes. Geology 41, 927–930.

Collettini, C., Tesei, T., Scuderi, M.M., Carpenter, B.M., Viti, C., 2019. Beyond Byerlee friction, weak faults and implications for slip behavior. Earth Planet Sci. Lett. 519, 245–263.

Coulomb, C.A., 1785, Mém. Math. Phys. (Paris): 161 p..

Cross, A.J., Prior, D.J., Stipp, M., Kidder, S., 2017. The recrystallized grain size piezometer for quartz: an EBSD-based calibration. Geophys. Res. Lett. 44, 6667–6674.

Cummins, P.R., Pranantyo, I.R., Pownall, J.M., Griffin, J.D., Meilano, I., Zhao, S., 2020. Earthquakes and tsunamis caused by low-angle normal faulting in the Banda Sea, Indonesia. Nat. Geosci. 13, 312–318.

Davis, G.H., 1987. A Shear-Zone Model for the Structural Evolution of Metamorphic Core Complexes in Southeastern Arizona, vol. 28. Geological Society, London, Special Publications, pp. 247–266.

Davis, G.A., Lister, G.S., Reynolds, S.J., 1986. Structural evolution of the Whipple and South Mountains shear zones, southwestern United States. Geology 14, 7–10.

Davis, G.H., Constenius, K.N., Dickinson, W.R., Rodríguez, E.P., Cox, L.J., 2004. Fault and fault-rock characteristics associated with Cenozoic extension and core-complex evolution in the Catalina-Rincon region, southeastern Arizona. Geol. Soc. Am. Bull. 116, 128–141.

Davis, G.H., Orent, E.B., Clinkscales, C., Ferroni, F.R., Gehrels, G.E., George, S.W.M., Guns, K.A., Hanagan, C.E., Hughes, A., Iriondo, A., 2023. Structural Analysis and Chronologic Constraints on Progressive Deformation within the Rincon Mountains, Arizona: Implications for Development of Metamorphic Core Complexes.

Demurtas, M., Fondriest, M., Balsamo, F., Clemenzi, L., Storti, F., Bistacchi, A., Di Toro, G., 2016. Structure of a normal seismogenic fault zone in carbonates: the Vado di Corno Fault, Campo Imperatore, Central Apennines (Italy). J. Struct. Geol. 90, 185–206.

Doglioni, C., Barba, S., Carminati, E., Riguzzi, F., 2014. Fault on–off versus coseismic fluids reaction. Geosci. Front. 5, 767–780.

Du, R., Xian, H., Wu, X., Zhu, J., Wei, J., Xing, J., Tan, W., He, H., 2021. Morphology dominated rapid oxidation of framboidal pyrite. Geochem. Perspectives Lett. 16, 53–58.

Dunn, J.G., De, G.C., O'Connor, B.H., 1989. The effect of experimental variables on the mechanism of the oxidation of pyrite: Part 2. Oxidation of particles of size 90–125 μm. Thermochim. Acta 155, 135–149.

Dusséaux, C., Gébelin, A., Boulvais, P., Ruffet, G., Poujol, M., Cogné, N., Branquet, Y., Mottram, C., Barou, F., Mulch, A., 2022. Timing and duration of meteoric water infiltration in the Quiberon detachment zone (Armorican Massif, Variscan belt, France). J. Struct. Geol. 156, 104546.

Ebert, A., Herwegh, M., Berger, A., Pfiffner, A., 2008. Grain coarsening maps for polymineralic carbonate mylonites: a calibration based on data from different Helvetic nappes (Switzerland). Tectonophysics 457, 128–142. https://doi.org/10.1016/j.tecto.2008.05.007.

Evans, J.P., Prante, M.R., Janecke, S.U., Ault, A.K., Newell, D.L., 2014. Hot faults: iridescent slip surfaces with metallic luster document high-temperature ancient seismicity in the Wasatch fault zone, Utah, USA. Geology 42, 623–626.

Faulkner, D.R., Mitchell, T.M., Behnsen, J., Hirose, T., Shimamoto, T., 2011. Stuck in the mud? Earthquake nucleation and propagation through accretionary forearcs. Geophys. Res. Lett. 38.

Ferri, F., Di Toro, G., Hirose, T., Han, R., Noda, H., Shimamoto, T., Quaresimin, M., de Rossi, N., 2011. Low-to high-velocity frictional properties of the clay-rich gouges from the slipping zone of the 1963 Vaiont slide, northern Italy. J. Geophys. Res. Solid Earth 116.

Ferrill, D.A., Morris, A.P., Evans, M.A., Burkhard, M., Groshong Jr, R.H., Onasch, C.M., 2004. Calcite twin morphology: a low-temperature deformation geothermometer. J. Struct. Geol. 26, 1521–1529.

Fletcher, J.M., Oskin, M.E., Teran, O.J., 2016. The role of a keystone fault in triggering the complex El Mayor–Cucapah earthquake rupture. Nat. Geosci. 9, 303–307.

Floyd, J.S., Mutter, J.C., Goodliffe, A.M., Taylor, B., 2001. Evidence for fault weakness and fluid flow within an active low-angle normal fault. Nature 411, 779–783.

Fondriest, M., Smith, S.A.F., Di Toro, G., Zampieri, D., Mittempergher, S., 2012. Fault zone structure and seismic slip localization in dolostones, an example from the Southern Alps, Italy. J. Struct. Geol. 45, 52–67.

Forster, M.A., Lister, G.S., 1999. Detachment Faults in the Aegean Core Complex of Ios, vol. 154. Geological Society, London, Special Publications, Cyclades, Greece, pp. 305–323.

Fossen, H., 2016. Structural Geology. Cambridge university press.

Fossen, H., Cavalcante, G.C.G., 2017. Shear zones–A review. Earth Sci. Rev. 171, 434–455.

Fricke, H.C., Wickham, S.M., O'Neil, J.R., 1992. Oxygen and hydrogen isotope evidence for meteoric water infiltration during mylonitization and uplift in the Ruby Mountains-East Humboldt Range core complex, Nevada. Contrib. Mineral. Petrol. 111, 203–221.

Fridrich, C.J., Thompson, R.A., 2011. Cenozoic Tectonic Reorganizations of the Death Valley Region, Southeast California and Southwest Nevada, vol. 1738. U.S. Geological Survey Professional Paper, p. 36.

Fridrich, C.J., Thompson, R.A., Slate, J.L., Berry, M.E., Machette, M.N., 2012. Geologic Map of the Southern Funeral Mountains Including Nearby Groundwater Discharge Sites in Death Valley National Park, California and Nevada, vol. 3151. U.S. Geological Survey Pamphlet and Scientific Investigations Map, p. 1:50. https://doi.org/10.3133/sim3151, 000.

Gébelin, A., Teyssier, C., Heizler, M.T., Mulch, A., 2015. Meteoric water circulation in a rolling-hinge detachment system (northern Snake Range core complex, Nevada). GSA Bulletin 127, 149–161.

Gresseth, J.L.S., Osmundsen, P.T., Péron-Pinvidic, G., 2023. 3D evolution of detachment fault systems in necking domains: insights from the Klakk Fault Complex and the Frøya High, mid-Norwegian rifted margin. Tectonics 42, e2022TC007600.

Hacker, B.R., Yin, A., Christie, J.M., Snoke, A.W., 1990. Differential stress, strain rate, and temperatures of mylonitization in the Ruby Mountains, Nevada: implications for the rate and duration of uplift. J. Geophys. Res. Solid Earth 95, 8569–8580.

Haines, S.H., van der Pluijm, B.A., 2010. Dating the detachment fault system of the Ruby Mountains, Nevada: significance for the kinematics of low-angle normal faults. Tectonics v. 29.

Haines, S.H., van der Pluijm, B.A., 2012. Patterns of mineral transformations in clay gouge, with examples from low-angle normal fault rocks in the western USA. J. Struct. Geol. 43, 2–32.

Haines, S.H., Kaproth, B., Marone, C., Saffer, D., Van der Pluijm, B., 2013. Shear zones in clay-rich fault gouge: a laboratory study of fabric development and evolution. J. Struct. Geol. 51, 206–225.

Haines, S., Marone, C., Saffer, D., 2014. Frictional properties of low-angle normal fault gouges and implications for low-angle normal fault slip. Earth Planet Sci. Lett. 408, 57–65.

Haines, S., Lynch, E., Mulch, A., Valley, J.W., van der Pluijm, B., 2016. Meteoric Fluid Infiltration in Crustal-Scale Normal Fault Systems as Indicated by δ18O and δ2H Geochemistry and 40Ar/39Ar Dating of Neoformed Clays in Brittle Fault Rocks: Lithosphere, vol. 8, pp. 587–600.

Hamilton, W.B., 1988. Detachment Faulting in the Death Valley Region, California and Nevada: Geologic and Hydrologic Investigations of a Potential Nuclear Waste Disposal Site at Yucca Mountain, Southern Nevada, vol. 1790. U.S. Geological Survey Bulletin, pp. 51–85.

Han, R., Shimamoto, T., Ando, J., Ree, J.-H., 2007a. Seismic Slip Record in Carbonate-Bearing Fault Zones: an Insight from High-Velocity Friction Experiments on Siderite Gouge: Geology, vol. 35, pp. 1131–1134.

Han, R., Shimamoto, T., Hirose, T., Ree, J.-H., Ando, J., 2007b. Ultralow friction of carbonate faults caused by thermal decomposition. Science 316, 878–881.

Han, R., Hirose, T., Shimamoto, T., 2010. Strong velocity weakening and powder lubrication of simulated carbonate faults at seismic slip rates. J. Geophys. Res. Solid Earth 115.

Hansman, R.J., Albert, R., Gerdes, A., Ring, U., 2018. Absolute Ages of Multiple Generations of Brittle Structures by U-Pb Dating of Calcite: Geology, vol. 46, pp. 207–210.

den Hartog, S.A.M., Spiers, C.J., 2013. Influence of subduction zone conditions and gouge composition on frictional slip stability of megathrust faults. Tectonophysics v. 600, 75–90.

den Hartog, S.A.M., Niemeijer, A.R., Spiers, C.J., 2012a. New Constraints on Megathrust Slip Stability under Subduction Zone P–T Conditions: Earth and Planetary Science Letters, vol. 353, pp. 240–252.

den Hartog, S.A.M., Peach, C.J., de Winter, D.A.M., Spiers, C.J., Shimamoto, T., 2012b. Frictional properties of megathrust fault gouges at low sliding velocities: new data on effects of normal stress and temperature. J. Struct. Geol. 38, 156–171.

den Hartog, S.A.M., Niemeijer, A.R., Spiers, C.J., 2013. Friction on Subduction Megathrust Faults: beyond the Illite–Muscovite Transition: Earth and Planetary Science Letters, vol. 373, pp. 8–19.

Heilbronner, R., Kilian, R., 2017. The grain size (s) of Black Hills Quartzite deformed in the dislocation creep regime. Solid Earth 8, 1071–1093.

Hirth, G., Tullis, J.A.N., 1992. Dislocation creep regimes in quartz aggregates. J. Struct. Geol. 14, 145–159.

Hobbs, B.E., Ord, A., Teyssier, C., 1986. Earthquakes in the ductile regime? Pure Appl. Geophys. 124, 309–336.

Hoisch, T.D., Simpson, C., 1993. Rise and tilt of metamorphic rocks in the lower plate of a detachment fault in the Funeral Mountains, Death Valley, California. J. Geophys. Res. Solid Earth 98, 6805–6827.

Hoisch, T.D., Wells, M.L., Beyene, M.A., Styger, S., Vervoort, J.D., 2014. Jurassic Barrovian metamorphism in a western US Cordilleran metamorphic core complex. Funeral Mountains, California: Geology 42, 399–402.

Holm, D.K., Dokka, R.K., 1991. Major Late Miocene cooling of the middle crust associated with extensional orogenesis in the Funeral Mountains, California. Geophys. Res. Lett. 18, 1775–1778. https://doi.org/10.1029/91GL02079.

Hu, G., Dam-Johansen, K., Wedel, S., Hansen, J.P., 2006. Decomposition and oxidation of pyrite. Prog. Energy Combust. Sci. 32, 295–314.

Huang, F., Zhang, L., Yi, B., Xia, Z., Zheng, C., 2015. Effect of H2O on pyrite transformation behavior during oxy-fuel combustion. Fuel Process. Technol. 131, 458–465.

Jia, Z., Jin, Z., Marchandon, M., Ulrich, T., Gabriel, A.-A., Fan, W., Shearer, P., Zou, X., Rekoske, J., Bulut, F., 2023. The complex dynamics of the 2023 Kahramanmaraş, Turkey, M w 7.8-7.7 earthquake doublet. Science 381, 985–990.

Jorgensen, F.R.A., Moyle, F.J., 1982. Phases formed during the thermal analysis of pyrite in air. J. Therm. Anal. Calorim. 25, 473–485.

Kaneki, S., Hirono, T., 2019. Diagenetic and shear-induced transitions of frictional strength of carbon-bearing faults and their implications for earthquake rupture dynamics in subduction zones. Sci. Rep. 9, 7884.

Kaneki, S., Oohashi, K., Hirono, T., Noda, H., 2020. Mechanical amorphization of synthetic fault gouges during rotary-shear friction experiments at subseismic to seismic slip velocities. J. Geophys. Res. Solid Earth 125, e2020JB019956.

Kaneko, Y., Lapusta, N., 2010. Supershear transition due to a free surface in 3-D simulations of spontaneous dynamic rupture on vertical strike-slip faults. Tectonophysics 493, 272–284.

Kennedy, L.A., White, J.C., 2001. Low-temperature Recrystallization in Calcite: Mechanisms and Consequences: Geology, vol. 29, pp. 1027–1030.

Kim, H.N., So, B.-D., Kim, M.S., Han, K.S., Oh, S.B., 2021. Seismic Fault Weakening via CO2 Pressurization Enhanced by Mechanical Deformation of Dolomite Fault Gouges: Geology, vol. 49, pp. 1245–1249.

Koch, N., Masch, L., 1992. Formation of alpine mylonites and pseudotachylytes at the base of the silvretta nappe, eastern alps. Tectonophysics 204, 289–306.

Labotka, T.C., 1980. Petrology of a medium-pressure regional metamorphic terrane, Funeral Mountains, California. Am. Mineral. 65, 670–689.

Lacey, H., 2018. The Properties and Role of Carbonate Cementation in Fault Zones [Ph. D]. Imperial College London, p. 229.

Levy, D.A., Zuza, A.V., Haproff, P.J., Odlum, M.L., 2021. Early Permian tectonic evolution of the Last Chance thrust system: an example of induced subduction initiation along a plate boundary transform. Geol. Soc. Am. Bull. 133, 1105–1127.

Lima, R.D., Hayman, N.W., Miranda, E., 2019. Rheological Inheritance: Lessons from the Death Valley Region, US Basin and Range Province, vol. 470. Geological Society, London, Special Publications, pp. 173–204.

Lin, A., 2008. Seismic slip in the lower crust inferred from granulite-related pseudotachylyte in the Woodroffe thrust, Central Australia. Pure Appl. Geophys. 165, 215–233.

Lin, A., Maruyama, T., Aaron, S., Michibayashi, K., Camacho, A., Kano, K., 2005. Propagation of seismic slip from brittle to ductile crust: evidence from pseudotachylyte of the Woodroffe thrust, central Australia. Tectonophysics 402, 21–35.

Lister, G.S., Davis, G.A., 1989. The origin of metamorphic core complexes and detachment faults formed during Tertiary continental extension in the northern Colorado River region, USA. J. Struct. Geol. 11, 65–94.

Lister, G.S., Snoke, A.W., 1984. SC mylonites. J. Struct. Geol. 6, 617–638.

Little, T.A., Webber, S.M., Mizera, M., Boulton, C., Oesterle, J., Ellis, S., Boles, A., van der Pluijm, B., Norton, K., Seward, D., 2019. Evolution of a rapidly slipping, active low-angle normal fault, Suckling-Dayman metamorphic core complex, SE Papua New Guinea. Bulletin 131, 1333–1363.

Liu, L., Liu, Q., Zhang, K., Zhang, S., Li, K., Li, J., Peng, G., 2023. Thermal decomposition and oxidation of pyrite with different morphologies in the coal gangue of North China. J. Therm. Anal. Calorim. 148, 2023–2038.

Logan, J.M., 1979. Experimental studies of simulated gouge and their application to studies of natural fault gouge. Analysis of Actual Fault Zones in Bedrock, pp. 305–343.

Long, S.P., Walker, J.P., 2015. Geometry and kinematics of the Grant Range brittle detachment system, eastern Nevada, USA: an end-member style of upper crustal extension. Tectonics 34, 1837–1862.

Lutz, B., Ketcham, R.A., Axen, G.J., Beyene, M.A., Wells, M.L., van Wijk, J.W., Stockli, D. F., Ross, J.I., 2021. Thermo-kinematic modeling of detachment-dominated extension, northeastern Death Valley area, USA: implications for mid-crustal thermal-rheological evolution. Tectonophysics 808. https://doi.org/10.1016/j.tecto.2021.228755.

Mariani, E., Mecklenburgh, J., Faulkner, D.R., 2015. Towards an Improved Understanding of the Mechanical Properties and Rheology of the Lithosphere: an

Introductory Article to 'Rock Deformation from Field, Experiments and Theory: A Volume in Honour of Ernie Rutter', vol. 409. Special Publications, pp. 1–18.

Masoch, S., Fondriest, M., Preto, N., Secco, M., Di Toro, G., 2019. Seismic cycle recorded in cockade-bearing faults (Col de Teghime, Alpine Corsica). J. Struct. Geol. 129, 103889.

Massironi, M., Bistacchi, A., Menegon, L., 2011. Misoriented faults in exhumed metamorphic complexes: rule or exception? Earth Planet Sci. Lett. 307, 233–239.

Melosh, B.L., Rowe, C.D., Gerbi, C., Smit, L., Macey, P., 2018. Seismic cycle feedbacks in a mid-crustal shear zone. J. Struct. Geol. 112, 95–111.

Monigle, P.W., Nabelek, J., Braunmiller, J., Carpenter, N.S., 2012. Evidence for low-angle normal faulting in the pumqu-xianza rift, tibet. Geophys. J. Int. 190, 1335–1340.

Moore, D.E., Summers, R., Byerlee, J.D., 1989. Sliding behavior and deformation textures of heated illite gouge. J. Struct. Geol. 11, 329–342.

Morrison, J., 1994. Meteoric water-rock interaction in the lower plate of the Whipple Mountain metamorphic core complex, California. J. Metamorph. Geol. 12, 827–840.

Muller, W., Aerden, D., Halliday, A.N., 2000. Isotopic dating of strain fringe increments: duration and rates of deformation in shear zones. Science 288, 2195–2198.

Müller, M., Grasemann, B., Iglseder, C., 2010. Field and micro-structural record of fault rock evolution within a low-angle normal fault system (Kea, Greece). In: EGU General Assembly Conference Abstracts, p. 9302.

Nakamura, Y., Oohashi, K., Toyoshima, T., Satish-Kumar, M., Akai, J., 2015. Strain-induced amorphization of graphite in fault zones of the Hidaka metamorphic belt, Hokkaido, Japan. J. Struct. Geol. 72, 142–161.

Nakatani, M., Scholz, C.H., 2004. Frictional healing of quartz gouge under hydrothermal conditions: 1. Experimental evidence for solution transfer healing mechanism. J. Geophys. Res. Solid Earth 109.

Niemeijer, A.R., Collettini, C., 2014. Frictional properties of a low-angle normal fault under in situ conditions: thermally-activated velocity weakening. Pure Appl. Geophys. 171, 2641–2664.

Niemeijer, A.R., Spiers, C.J., 2007. A microphysical model for strong velocity weakening in phyllosilicate-bearing fault gouges. J. Geophys. Res. Solid Earth 112.

Niemi, N.A., 2012. Geologic Map of the Central Grapevine Mountains, Inyo County, California and Esmeralda and Nye Counties, vol. 12. Nevada: Geological Society of America Digital Map and Chart Series. https://doi.org/10.1130/2012.DMCH012.

Novellino, R., Prosser, G., Spiess, R., Viti, C., Agosta, F., Tavarnelli, E., Bucci, F., 2015. Dynamic weakening along incipient low-angle normal faults in pelagic limestones (Southern Apennines, Italy). J. Geol. Soc. 172, 283–286.

Ohl, M., Plümper, O., Chatzaras, V., Wallis, D., Vollmer, C., Drury, M., 2020. Mechanisms of fault mirror formation and fault healing in carbonate rocks. Earth Planet Sci. Lett. 530, 115886.

Okuda, H., Kitamura, M., Takahashi, M., Yamaguchi, A., 2023. Frictional properties of the décollement in the shallow Nankai Trough: constraints from friction experiments simulating in-situ conditions and implications for the seismogenic zone. Earth Planet Sci. Lett. 621, 118357.

Oohashi, K., Hirose, T., Shimamoto, T., 2011. Shear-induced graphitization of carbonaceous materials during seismic fault motion: experiments and possible implications for fault mechanics. J. Struct. Geol. 33, 1122–1134.

Oohashi, K., Han, R., Hirose, T., Shimamoto, T., Omura, K., Matsuda, T., 2014. Carbon-forming Reactions under a Reducing Atmosphere during Seismic Fault Slip: Geology, vol. 42, pp. 787–790.

Osmundsen, P.T., Ebbing, J., 2008. Styles of extension offshore mid-Norway and implications for mechanisms of crustal thinning at passive margins. Tectonics 27.

Pang, G., Koper, K.D., Mesimeri, M., Pankow, K.L., Baker, B., Farrell, J., Holt, J., Hale, J. M., Roberson, P., Burlacu, R., 2020. Seismic analysis of the 2020 Magna, Utah, earthquake sequence: evidence for a listric Wasatch fault. Geophys. Res. Lett. 47, e2020GL089798.

De Paola, N., Hirose, T., Mitchell, T., Di Toro, G., Viti, C., Shimamoto, T., 2011. Fault Lubrication and Earthquake Propagation in Thermally Unstable Rocks: Geology, vol. 39, pp. 35–38.

Passchier, C.W., Trouw, R.A.J., 2005. Microtectonics. Springer Verlag, Berlin.

Paterson, M.S., 2013. Deformation mechanisms: granular flow. In: Paterson, M.S. (Ed.), Materials Science for Structural Geology. Springer Netherlands, Dordrecht, pp. 209–243. https://doi.org/10.1007/978-94-007-5545-1_7.

Petit, J.P., 1987. Criteria for the sense of movement on fault surfaces in brittle rocks. J. Struct. Geol. 9, 597–608.

Delle Piane, C., Clennell, M. Ben, Keller, J.V.A., Giwelli, A., Luzin, V., 2017. Carbonate hosted fault rocks: a review of structural and microstructural characteristic with implications for seismicity in the upper crust. J. Struct. Geol. 103, 17–36.

Delle Piane, C., Piazolo, S., Timms, N.E., Luzin, V., Saunders, M., Bourdet, J., Giwelli, A., Ben Clennell, M., Kong, C., Rickard, W.D.A., 2018. Generation of Amorphous Carbon and Crystallographic Texture during Low-Temperature Subseismic Slip in Calcite Fault Gouge: Geology, vol. 46, pp. 163–166.

Pittarello, L., Pennacchioni, G., Di Toro, G., 2012. Amphibolite-facies pseudotachylytes in Premosello metagabbro and felsic mylonites (Ivrea Zone, Italy). Tectonophysics 580, 43–57.

Platt, J.P., 2023. A process-based theory for subgrain-size and grain-size piezometry. J. Struct. Geol. 177, 104987.

Platt, J.P., De Bresser, J.H.P., 2017. Stress dependence of microstructures in experimentally deformed calcite. J. Struct. Geol. 105, 80–87.

Platt, J.P., Vissers, R.L.M., 1980. Extensional structures in anisotropic rocks. J. Struct. Geol. 2, 397–410.

Platt, J.P., Behr, W.M., Cooper, F.J., 2015a. Metamorphic core complexes: windows into the mechanics and rheology of the crust. J. Geol. Soc. 172, 9–27.

Platt, J.D., Brantut, N., Rice, J.R., 2015b. Strain localization driven by thermal decomposition during seismic shear. J. Geophys. Res. Solid Earth 120, 4405–4433.

Price, N.A., Johnson, S.E., Gerbi, C.C., West Jr, D.P., 2012. Identifying deformed pseudotachylyte and its influence on the strength and evolution of a crustal shear zone at the base of the seismogenic zone: tectonophysics, 518, 63–83.

Ramsay, J.G., Graham, R.H., 1970. Strain variation in shear belts. Can. J. Earth Sci. 7, 786–813.

Rana, N., Bhattacharya, F., Basavaiah, N., Pant, R.K., Juyal, N., 2013. Soft sediment deformation structures and their implications for late quaternary seismicity on the south Tibetan detachment system, central Himalaya (Uttarakhand), India. Tectonophysics 592, 165–174.

Riedel, W., 1929. Zur mechanik geologischer Brucherscheinungen (Ein Beitrag zum Problem der Fiederspatten): Centralblatt für Mineralogie. Geologie und Paläontologie. B (1929), pp. 354-368.

Rietbrock, A., Tiberi, C., Scherbaum, F., Lyon-Caen, H., 1996. Seismic Slip on a Low Angle Normal Fault in the Gulf of Corinth: Evidence from High-resolution Cluster Analysis of Microearthquakes: Geophysical Research Letters, vol. 23, pp. 1817–1820.

Roberts, N.M.W., Holdsworth, R.E., 2022. Timescales of faulting through calcite geochronology: a review. J. Struct. Geol. 158, 104578.

Roberts, N.M.W., Walker, R.J., 2016. U-Pb geochronology of calcite-mineralized faults: absolute timing of rift-related fault events on the northeast Atlantic margin. Geology 44, 531–534.

Rowe, C.D., Griffith, W.A., 2015. Do faults preserve a record of seismic slip: a second opinion. J. Struct. Geol. 78, 1–26.

Rowe, C.D., Fagereng, Å., Miller, J.A., Mapani, B., 2012a. Signature of coseismic decarbonation in dolomitic fault rocks of the Naukluft Thrust, Namibia. Earth Planet Sci. Lett. 333, 200–210.

Rowe, C.D., Kirkpatrick, J.D., Brodsky, E.E., 2012b. Fault rock injections record paleo-earthquakes. Earth Planet Sci. Lett. 335, 154–166.

Saffer, D.M., Marone, C., 2003. Comparison of smectite-and illite-rich gouge frictional properties: application to the updip limit of the seismogenic zone along subduction megathrusts. Earth Planet Sci. Lett. 215, 219–235.

Scholz, C.H., 1988. The critical slip distance for seismic faulting. Nature 336, 761–763.

Scholz, C.H., 2019. The Mechanics of Earthquakes and Faulting. Cambridge university press.

Searle, M.P., 2010. Low-angle normal faults in the compressional himalayan orogen; evidence from the annapurna–dhaulagiri himalaya, Nepal. Geosphere 6, 296–315.

Selverstone, J., Axen, G.J., Bartley, J.M., 1995. Fluid inclusion constraints on the kinematics of footwall uplift beneath the Brenner Line normal fault, eastern Alps. Tectonics 14, 264–278.

Selverstone, J., Axen, G.J., Luther, A., 2012. Fault localization controlled by fluid infiltration into mylonites: formation and strength of low-angle normal faults in the midcrustal brittle-plastic transition. J. Geophys. Res. Solid Earth 117.

Shimamoto, T., 1989. The origin of SC mylonites and a new fault-zone model. J. Struct. Geol. 11, 51–64.

Sibson, R.H., 1980. Transient discontinuities in ductile shear zones. J. Struct. Geol. 2, 165–171.

Sibson, R.H., 1992. Implications of fault-valve behaviour for rupture nucleation and recurrence. Tectonophysics 211, 283–293.

Sibson, R.H., 2019. Arterial faults and their role in mineralizing systems. Geosci. Front. 10, 2093–2100.

Simpson, C., Schmid, S.M., 1983. An evaluation of criteria to deduce the sense of movement in sheared rocks. Geol. Soc. Am. Bull. 94, 1281–1288.

Singleton, J.S., Wong, M.S., Johnston, S.M., 2018. The Role of Calcite-Rich Metasedimentary Mylonites in Localizing Detachment Fault Strain and Influencing the Structural Evolution of the Buckskin-Rawhide Metamorphic Core Complex, West-Central Arizona: Lithosphere, vol. 10, pp. 172–193.

Smeraglia, L., Bettucci, A., Billi, A., Carminati, E., Cavallo, A., Di Toro, G., Natali, M., Passeri, D., Rossi, M., Spagnuolo, E., 2017a. Microstructural evidence for seismic and aseismic slips along clay-bearing, carbonate faults. J. Geophys. Res. Solid Earth 122, 3895–3915.

Smeraglia, L., Billi, A., Carminati, E., Cavallo, A., Doglioni, C., 2017b. Field-to nano-scale evidence for weakening mechanisms along the fault of the 2016 Amatrice and Norcia earthquakes, Italy. Tectonophysics 712, 156–169.

Smeraglia, L., Bernasconi, S.M., Berra, F., Billi, A., Boschi, C., Caracausi, A., Carminati, E., Castorina, F., Doglioni, C., Italiano, F., 2018. Crustal-scale fluid circulation and co-seismic shallow comb-veining along the longest normal fault of the central Apennines, Italy. Earth Planet Sci. Lett. 498, 152–168.

Smith, S.A.F., Billi, A., Toro, G. Di, Spiess, R., 2011. Principal slip zones in limestone: microstructural characterization and implications for the seismic cycle (Tre Monti Fault, Central Apennines, Italy). Pure Appl. Geophys. 168, 2365–2393.

Smith, S.A.F., Di Toro, G., Kim, S., Ree, J.-H., Nielsen, S., Billi, A., Spiess, R., 2013. Coseismic recrystallization during shallow earthquake slip. Geology 41, 63–66.

Smith, S.A.F., Nielsen, S., Di Toro, G., 2015. Strain localization and the onset of dynamic weakening in calcite fault gouge. Earth Planet Sci. Lett. 413, 25–36.

Snow, J.K., 1992. Large-magnitude Permian shortening and continental-margin tectonics in the southern Cordillera. Geol. Soc. Am. Bull. 104, 80–105.

Snow, J.K., Wernicke, B.P., 2000. Cenozoic tectonism in the central basin and range: magnitude, rate, and distribution of upper crustal strain. Am. J. Sci. 300, 659–719. https://doi.org/10.2475/ajs.300.9.659.

Del Sole, L., Mazzoli, S., Carafa, M.M.C., Toffol, G., Pennacchioni, G., Giuli, G., Invernizzi, C., Tondi, E., 2023. Interseismic creep of carbonate-hosted seismogenic normal faults: insights from central Italy. GSA Bulletin 136, 1605–1627. https://doi.org/10.1130/B36954.1.

Spencer, J.E., Chase, C.G., 1989. Role of crustal flexure in initiation of low-angle normal faults and implications for structural evolution of the Basin and Range province. J. Geophys. Res. Solid Earth 94, 1765–1775.

Spencer, J.E., Reynolds, S.J., Scott, R.J., Richard, S.M., 2016. Shortening in the upper plate of the Buckskin-Rawhide extensional detachment fault, southwestern US, and implications for stress conditions during extension. Tectonics 35, 3119–3136.

Steacy, S., Gomberg, J., Cocco, M., 2005. Introduction to special section: stress transfer, earthquake triggering, and time-dependent seismic hazard. J. Geophys. Res. Solid Earth 110.

Stevens, C.H., Stone, P., 2005. Interpretation of the Last Chance thrust, Death Valley region, California, as an Early Permian décollement in a previously undeformed shale basin. Earth Sci. Rev. 73, 79–101.

Stipp, M., Tullis, J., 2003. The recrystallized grain size piezometer for quartz. Geophys. Res. Lett. 30.

Styron, R.H., Hetland, E.A., 2014. Estimated likelihood of observing a large earthquake on a continental low-angle normal fault and implications for low-angle normal fault activity. Geophys. Res. Lett. 41, 2342–2350.

Sulem, J., Famin, V., 2009. Thermal decomposition of carbonates in fault zones: slip-weakening and temperature-limiting effects. J. Geophys. Res. Solid Earth 114.

Tchalenko, J.S., 1970. Similarities between shear zones of different magnitudes. Geol. Soc. Am. Bull. 81, 1625–1640.

Tembe, S., Lockner, D.A., Wong, T., 2010. Effect of clay content and mineralogy on frictional sliding behavior of simulated gouges: binary and ternary mixtures of quartz, illite, and montmorillonite. J. Geophys. Res. Solid Earth 115.

Tesei, T., Collettini, C., Viti, C., Barchi, M.R., 2013. Fault architecture and deformation mechanisms in exhumed analogues of seismogenic carbonate-bearing thrusts. J. Struct. Geol. 55, 167–181.

Tesei, T., Collettini, C., Barchi, M.R., Carpenter, B.M., Di Stefano, G., 2014. Heterogeneous strength and fault zone complexity of carbonate-bearing thrusts with possible implications for seismicity. Earth Planet Sci. Lett. 408, 307–318.

Tesei, T., Lacroix, B., Collettini, C., 2015. Fault Strength in Thin-Skinned Tectonic Wedges across the Smectite-Illite Transition: Constraints from Friction Experiments and Critical Tapers: Geology, vol. 43, pp. 923–926.

Di Toro, G., Goldsby, D.L., Tullis, T.E., 2004. Friction falls towards zero in quartz rock as slip velocity approaches seismic rates. Nature 427, 436–439.

Twite, F., Nex, P., Kinnaird, J., 2020. Strain fringes and strain shadows at Kamoa (DRC), implications for copper mineralisation. Ore Geol. Rev. 122, 103536.

Vadacca, L., Casarotti, E., Chiaraluce, L., Cocco, M., 2016. On the mechanical behaviour of a low-angle normal fault: the Alto Tiberina fault (Northern Apennines, Italy) system case study. Solid Earth 7, 1537–1549.

Vauchez, A., 1987. The development of discrete shear-zones in a granite: stress, strain and changes in deformation mechanisms. Tectonophysics 133, 137–156. https://doi.org/10.1016/0040-1951(87)90286-1.

Verberne, B.A., Niemeijer, A.R., De Bresser, J.H.P., Spiers, C.J., 2015. Mechanical behavior and microstructure of simulated calcite fault gouge sheared at 20–600 C: Implications for natural faults in limestones. J. Geophys. Res. Solid Earth 120, 8169–8196.

Volpe, G., Pozzi, G., Collettini, C., 2022. YBPR or SCC'? Suggestion for the nomenclature of experimental brittle fault fabric in phyllosilicate-granular mixtures. J. Struct. Geol. 165, 104743.

Wang, K., Bilek, S.L., 2014. Invited review paper: fault creep caused by subduction of rough seafloor relief. Tectonophysics 610, 1–24.

Wernicke, B., 1981. Low-angle normal faults in the Basin and Range Province: nappe tectonics in an extending orogen. Nature 291, 645–648.

Wernicke, B., 1992. Cenozoic extensional tectonics of the US Cordillera. In: Burchfiel, B. C., Lipman, P.W., Zoback, M.L. (Eds.), The Cordilleran Orogen: Coterminous U.S. Geological Society of America, the Geology of North America, v. G-3, Boulder, Colorado, pp. 553–581. https://doi.org/10.1130/DNAG-GNA-G3.553.

Wernicke, B., 1995. Low-angle normal faults and seismicity: a review. J. Geophys. Res. Solid Earth 100, 20159–20174.

Westaway, R., 1999. The mechanical feasibility of low-angle normal faulting. Tectonophysics 308, 407–443.

Whitney, D.L., Teyssier, C., Rey, P., Buck, W.R., 2013. Continental and oceanic core complexes. GSA Bulletin 125, 273–298. https://doi.org/10.1130/B30754.1.

Wiest, J.D., Fossen, H., Jacobs, J., 2020. Shear zone evolution during core complex exhumation–Implications for continental detachments. J. Struct. Geol. 140, 104139.

Workman, J.B., Menges, C., Fridrich, C.J., Thompson, R.A., 2016. Geologic Map of Death Valley National Park, Nevada and California. Geological Society of America Annual Meeting, Denver, Colorado. https://doi.org/10.1130/abs/2016AM-286651.

Wright, L.A., Troxel, B.W., 1993. Geologic Map of the Central and Northern Funeral Mountains and Adjacent Areas, Death Valley Region, Southern California, vol. 2305. U.S. Geological Survey Miscellaneous Investigations Map, 1:48,000.

Wust, S.L., 1986. Regional correlation of extension directions in Cordilleran metamorphic core complexes. Geology 14, 828–830.

Yin, A., 1989. Origin of regional, rooted low-angle normal faults: a mechanical model and its tectonic implications. Tectonics 8, 469–482.

Yin, C., Zhang, B., Han, B.-F., Zhang, J., Wang, Y., Ai, S., 2017. Structural analysis and deformation characteristics of the Yingba metamorphic core complex, northwestern margin of the North China craton, NE Asia. J. Struct. Geol. 94, 195–212.

Zhu, J., Xian, H., Lin, X., Tang, H., Du, R., Yang, Y., Zhu, R., Liang, X., Wei, J., Teng, H. H., 2018. Surface structure-dependent pyrite oxidation in relatively dry and moist air: implications for the reaction mechanism and sulfur evolution. Geochem. Cosmochim. Acta 228, 259–274.